Detonation Shock Dynamics Modeling and Calibration of the HMX-Based Conventional High Explosive PBX 9501 with Application to the Two-Dimensional Circular Arc Geometry

Carlos Chiquete, Mark Short*, Stephen J. Voelkel, Eric K. Anderson, Scott I. Jackson

Los Alamos National Laboratory, New Mexico, NM 87545, USA

Abstract

A surface evolution model is developed for the detonation propagation dynamics of the HMX-based conventional high explosive PBX 9501, which relates the normal surface speed D_n to its local surface curvature κ. Such surface evolution models are important for the understanding and modification of engineering design calculations for high explosive applications. We describe a series of unconfined PBX 9501 slab geometry experiments of varying thickness, and detail how the steady axial detonation speed and detonation front shape data are obtained. A merit-function based calibration process is then described that uses both the PBX 9501 thickness effect and front shape data to parametrize the $D_n - \kappa$ propagation law. The time-dependent PBX 9501 $D_n - \kappa$ surface evolution law is then applied to detonation wave propagation in two-dimensional circular arc geometries, systematically examining the effect of arc thickness, inner radius, relaxation dynamics to steady-state propagation and confinement.

1. Introduction

Detonations in either gaseous or heterogeneous condensed-phase explosives are chemically driven, supersonic shock waves. The detonation structure consists of a shock wave, supported by a region of chemical reaction, and followed by a region of product flow. Detonations in gases typically travel at speeds in the range of 1-2.5 km s^{-1}. In condensed-phase explosives, detonations travel in the range of 3-10 km s^{-1} depending on the energetics of the material, and can generate pressures in the range of 10-35 GPa. At these pressures, the condensed-phase or high explosive (HE) behaves as an inviscid fluid [1]. Unlike gases, detonations in condensed-phase explosives are also hydrodynamically stable, although their spatial structure often contains an imprint of the underlying degree of material heterogeneity. Detonations in condensed-phase explosives are primarily used to drive various confiner materials, typically metals, surrounding the HE for mining, munitions and other applications [2]. From a modeling viewpoint, this requires prediction of both the motion of the detonation in an HE in often complex geometries, including the influence of the specific confinement properties, and the energy imparted by the HE to the surrounding material, which drives its subsequent evolution. The former is known as the timing problem, and the latter the energy delivery problem.

---

*Corresponding author

Two types of basic models exist for condensed-phase HE detonation. Reactive burn models resolve the detonation reaction zone explicitly. However, such models provide a significant challenge for computational modeling due to the several orders of magnitude scale disparity between the detonation reaction zone thickness (of the order of a few 100s of microns for conventional HEs) and the larger length scales characterizing the explosive geometry. In order to avoid the need to resolve the fine length scales of the detonation reaction zone, a class of engineering models have been developed which calculate the detonation propagation path via a surface evolution description. This is then combined with various methods for calculating the energy delivery to the surrounding confinement. The combination is known as program (or programmed) burn methods. The current paper is concerned with advanced methods for the program burn timing component for detonation propagation in a conventional condensed-phase explosive.

Original surface evolution descriptions for detonation propagation were based on a Huygens construction, in which the normal speed of the surface is assumed to be constant (typically taken to be the Chapman-Jouguet detonation speed). This would be an appropriate assumption if the detonation reaction zone was vanishingly thin [3]. It does not account for the effects on the propagation behavior of the finite reaction zone length of the detonation or the effects of the material properties of the HE confinement. Nonetheless, this approach has been utilized in a number of explosive problems including astrophysical supernova detonation [4, 5, 6], rock fragmentation due to explosive detonation loading in mining [7, 8], calculation of explosively-driven air blast effects [9, 10], and modeling of explosive shaped charges [11].

In reality, detonation motion is highly dependent on the local curvature of the detonation front that develops both due to the geometry and confinement effects. In order to account for these effects, the concept of Detonation Shock Dynamics (DSD) was developed [12, 13, 14, 15]. This replaces the detonation shock front and reaction zone with an intrinsic propagated surface in which the normal surface speed D_n is a function of the local surface curvature κ. The DSD model is motivated by an asymptotic analysis of detonation wave motion under the assumptions of a quasi-steady evolution of the detonation front, i.e. the characteristic particle transit time through the reaction zone is short compared to the evolution timescale of the surface shape, and that the local curvature of the front is small compared to the inverse of the reaction zone length scale [12]. Under these assumptions, the normal surface velocity is then a function only of its local curvature (known also as a $D_n - \kappa$ law). In the DSD model, the effect on the surface evolution of the density and impedance properties of the material confining the HE is incorporated by enforcing a particular surface angle (edge angle) on the wave shape at the interface between the explosive and confining material. The specification of the edge angle serves as the boundary condition constraint in the DSD surface wave calculation. Some examples of the application of DSD models include [16, 17, 18, 19, 20, 21, 22, 23].

The $D_n - \kappa$ relation for a particular HE is usually obtained through experimental calibration. The calibration experiments utilize explosive charges in either unconfined, cylindrically symmetric (rate-stick) or large-aspect-ratio rectangular cuboid (slab) geometries as illustrated in Fig. 1. The charge is initiated at one end and the progress of the resulting detonation wave is tracked axially. For cylinders or slabs with a sufficiently large aspect ratio, the detonation achieves a steady-state propagation with a certain axial phase speed. For condensed-phase explosives, rate-stick experiments performed for multiple charge diameters have shown that the steady phase speed monotonically decreases with decreasing charge radius [25] (termed the diameter effect). A similar behavior holds for the slab geometry, analogously termed the thickness effect [26]. The reason for this is that the intense pressures (often many 10s of GPa) generated in the detonation products force a lateral

2

T D_0 κ_s

(a) Slab

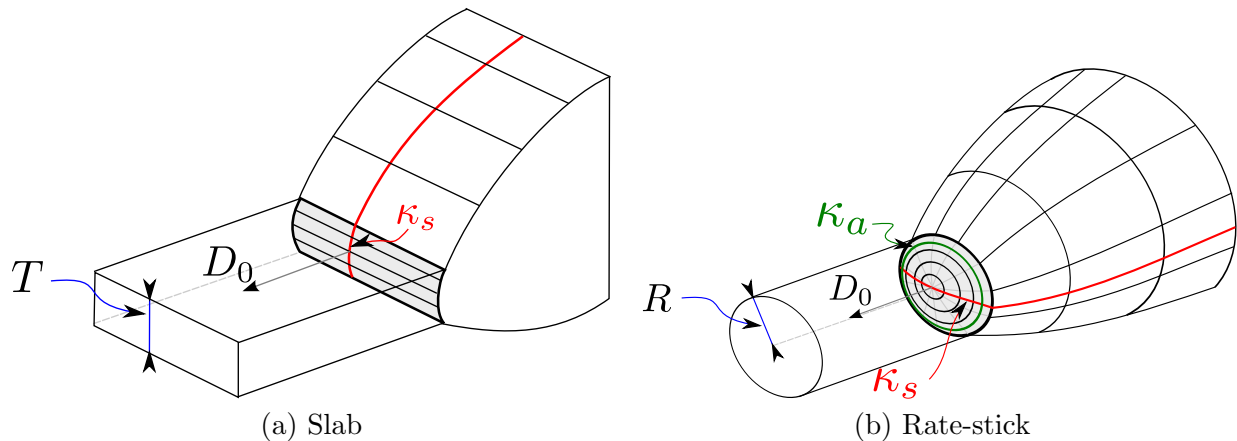κ_a R D_0 κ_s

(b) Rate-stick

Figure 1: Schematic of detonation front shapes in slab and rate-stick HE calibration geometries. The detonation front surface curvature components are denoted for both geometries, i.e. the slab component κ_s (——) and axisymmetric component κ_a (——), where the rate-stick test contains both components. Both curvature components vary as a function of distance from the geometry center. These schematic figures are based on those originally shown in [24].

movement in the product flow. The resulting streamline divergence in the post-shock flow induces a curved detonation front, which reduces the amount of energy that directly sustains the detonation shock. Smaller charges increase the streamline divergence and detonation shock surface curvature, yielding monotonically decreasing phase speeds. The increasing detonation shock surface curvature with decreasing charge width is revealed in detonation front shape measurements. These are usually obtained by recording the time-of-arrival of the detonation shock along a breakout surface through high-speed streak camera imaging [25, 27]. The rate-stick or slab geometry experiments for various charge sizes provide detonation phase speeds and shock shapes which can then be used to fit optimal parameters for the $D_n - \kappa$ surface motion relation of a given HE.

The present work describes the DSD model calibration of PBX 9501, a plastic bonded explosive (PBX) composed of 95.0 weight (wt.)% cyclotetramethylene-tetranitramine (HMX) explosive crystals, with a binder mixture of 2.5 wt.% Estane and a 2.5 wt.% eutectic mixture of bis(2,2-dinitropropyl)acetal and bis(2,2-dinitropropyl) formal (BDNPA/BDNPF). Its properties are similar to many other conventional HEs, and therefore our work on PBX 9501 is a surrogate for understanding the influence of curvature on other classes of conventional HEs. The characteristic heterogeneous grain structure of PBX 9501 is reproduced in Fig. 2 from Skidmore et al. [28, 29]. As noted, PBX 9501 is considered to be a conventional HE and most commonly used as either a main charge or as a booster for the initiation of insensitive high explosives [30, 26]. Detonations in PBX 9501 have a spatially small reaction zone of $\mathcal{O}(100\ \mu\text{m})$, a Chapman-Jouguet detonation speed of ≈ 8.8 mm/μs, and a rate-stick geometry failure diameter of around 1.52 mm [25]. Given that the detonation reaction zone length is characteristic of the scale of an HMX crystal (as illustrated in Fig. 2), significant imprinting of the heterogeneous grain structure on the detonation shock wave shape might be expected.

In the following, we describe experiments where detonation front shape data is extracted from six PBX 9501 slab tests of varying thickness. The thickness effect and newly obtained front shape data are then used to calibrate a new $D_n - \kappa$ relation for PBX 9501. As part of this process, we
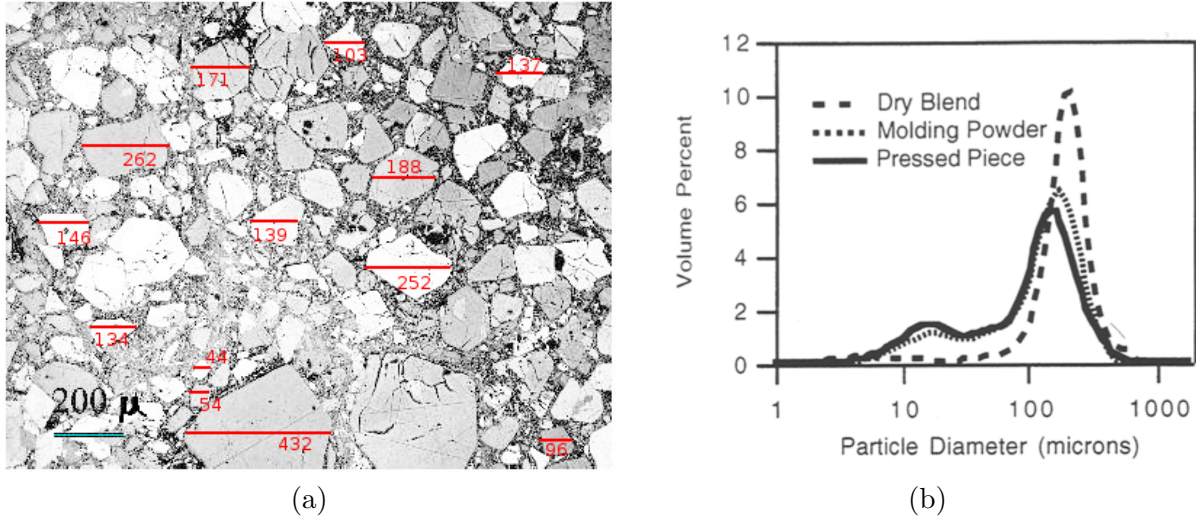
Figure 2: (a) Detail of the PBX 9501 grain structure (reproduced from [28] with permission). Note that the dominant grain size is on the order of 100 μm. The original image has been annotated here with the characteristic dimensions of a selection of HMX grains ranging from 100–450 μm (in red). (b) The distribution in volume percent vs. particle diameter for HMX grains in pressed PBX 9501 (solid black line) (reproduced from [29] with permission). The main peak of the distribution is $\mathcal{O}(100)$ μms.

examine the origin of the smaller length scale of explosive heterogeneity on the longer length scale of the mean surface curvature variation. We then apply the $D_n - \kappa$ relation to examine the properties of PBX 9501 detonation in a two-dimensional circular arc geometry. In a related publication by Short et al. [23], three validation experiments were described that explored PBX 9501 detonation in a two-dimensional circular arc geometry with varying arc thickness and inner arc surface radius. Detonation propagation in a circular arc has attracted significant attention recently in gaseous explosives [31, 32, 33, 34], due to its application to rotating detonation engines, and in condensed-phase explosives including both experimental [35, 36, 37] and simulation [21, 38, 39, 40] studies, as it is the simplest geometry that accounts for modifications of the detonation front curvature induced by diffraction. In the current paper, we compare solutions of our new PBX 9501 DSD model applied to the arc geometries in [23] with those determined experimentally. Excellent agreement of both the linear speeds on the inner and outer arc surfaces are found, as well as those of the detonation front shapes predicted by the DSD model, for all three PBX 9501 arc geometries. This provides validation of our DSD model. Finally, we explore PBX 9501 detonation properties for the circular arc geometry using the newly derived DSD relation, including the effect of changes in arc thickness, inner radius and confinement, and of the relaxation dynamics to steady-state propagation.

2. PBX 9501 Slab Geometry Experiments

The properties of steady, axially propagating PBX 9501 detonation have been calculated in a series of unconfined large-aspect-ratio, rectangular-cuboid HE charges (slabs). The detonation speeds have been previously reported in [26]. The slab geometry is intended to generate a region of steady, two-dimensional planar flow around the charge centerline (Fig. 1a and Fig. 3). As the detonation wave propagates through the slab, expansion waves originating from HE/air interfaces
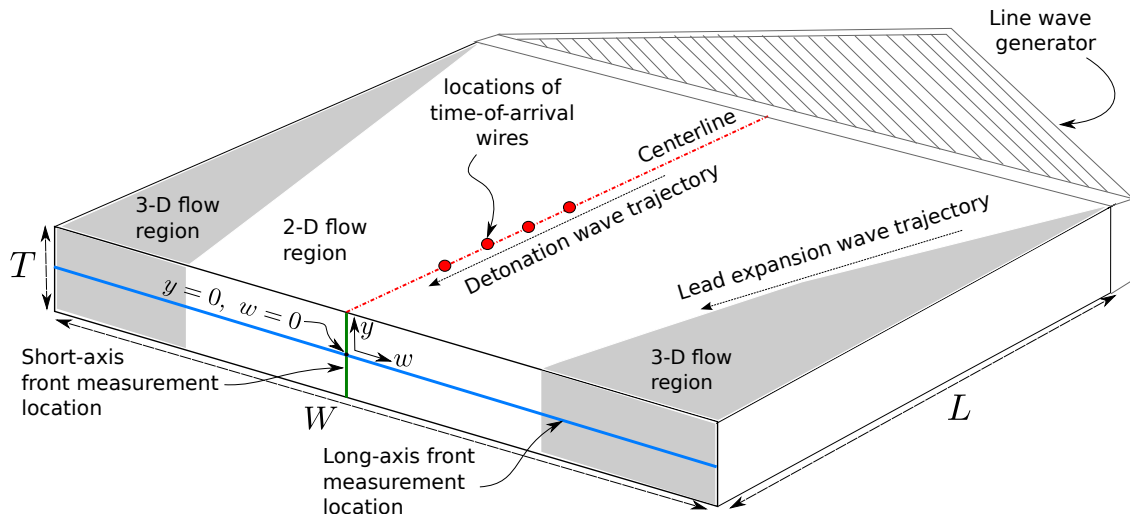
Figure 3: Slab geometry experimental schematic showing the front measurement locations and some of the time of arrival wire locations along the charge centerline. Two-dimensional planar flow is established in the central region of the slab in the direction represented by T.

propagate inward along the short- and long-axis directions (i.e. along the T and W directions in Fig. 3). The waves that propagate along the short-axis direction subsequently establish the desired 2D planar flow. Expansion waves propagating along the long-axis direction combine with the short-axis disturbances to produce a fully 3D flow region which grows towards the centerline. Consequently, the slab dimensions must be chosen to ensure that the 3D flow regions do not arrive at the charge centerline prior to the arrival of the 2D planar detonation structure at the end of the charge [26]. This is achieved by limiting the charge length (L in Fig. 3) relative to the charge-width W. The charge length must also be sufficient to ensure a steady detonation propagation regime is fully established. A distance of 4-5 times the charge thickness (T) is typically required for transient behavior resulting from the initiation of the main explosive charge (PBX 9501) to dissipate.

2.1. Detonation speed data, front shape imaging and curvature analysis

The various PBX 9501 slab dimensions, densities and steady axial detonation phase speeds (D_0) are listed in Table 1. The phase speed data is plotted in Fig. 4 as a thickness effect curve, where the horizontal axis is the inverse slab thickness ($1/T$). As expected, decreasing charge thickness leads to a monotonically decreasing phase speed. In terms of experimental shot-to-shot variability, the three tests conducted for $T = 3.00$ mm have a maximum to minimum D_0 variation of 28 m/s, with the two $T = 3.00$ mm tests conducted at the same reported density of 1.832 g/cm^3 possessing a D_0 variation of 15 m/s. Note that the density variation within the slab geometry tests is in the range of 1.8295–1.8334 g/cm^3, a difference of 0.0039 g/cm^3. Thus, given the closeness of the manufactured slab densities, we do not attempt to isolate any potential effect of density variations in the following analysis.

The detonation shape at the end of the charge along the centerline slab height direction (T in Fig. 3) was measured for the 1.00, 1.98, 3.00 (test # 8-1691), 3.99, 6.00 and 8.01 mm thickness tests. A mirror destruction technique was used to image the detonation breakout times [25, 27],

Shot number	T (mm)	L (mm)	W (mm)	ρ_0 (g/cc)	D_0 (mm/μs)	$\pm SE(D_0)$ (mm/μs)
8-1705	1.00	130.0	150.0	1.831	8.461	0.003
8-1701	1.98	130.0	150.0	1.8311	8.687	0.001
8-1595	3.00	135.0	151.2	1.832	8.738	0.006
8-1646	3.00	135.0	151.2	1.832	8.723	0.004
8-1691	3.00	135.0	151.2	1.8334	8.751	0.002
8-1694	3.99	130.0	150.0	1.8309	8.755	0.002
8-1723	6.00	130.0	150.0	1.8297	8.766	0.001
8-1735	8.01	130.1	150.1	1.8295	8.777	0.003

Table 1: PBX 9501 slab experiment dimensions and thickness effect data. Data reproduced from Jackson and Short [26]. Densities ranged from 1.8295–1.8334 g/cm^3. SE represents the standard error of a straight line fit to the timing diagnostics.
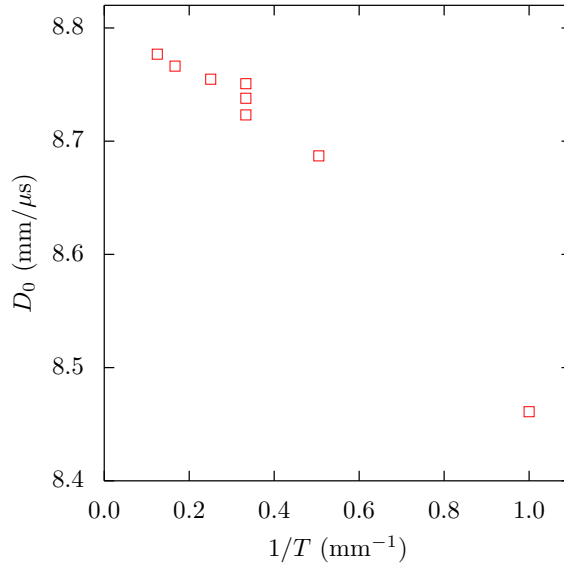

Figure 4: Thickness effect curve (detonation phase speed variation D_0 with $1/T$) for PBX 9501.

using a 0.6 μm aluminium coating deposited on a layer of polymethyl methacrylate (PMMA) as the mirror, which is attached to the front of the charge (Fig. 5a). At breakout, the mirrored surface is sequentially destroyed along a line from the charge center (represented by the coordinate location $y = 0$ in Fig. 3) to the charge edges ($y = \pm T/2$) in the T direction, i.e. along the green line shown in Fig. 3. A high-speed streak camera records the abrupt change in surface reflectivity. The local detonation wave breakout time across the charge thickness can then be inferred from the camera image. Figure 5b (right) shows the breakout streak image for the 6.00 mm thick slab with time increasing to the right. The edges of the charge are indicated by the horizontal green lines obtained from the initial fiducial image, which provides the camera/lens spatial magnification scale (Fig. 5b
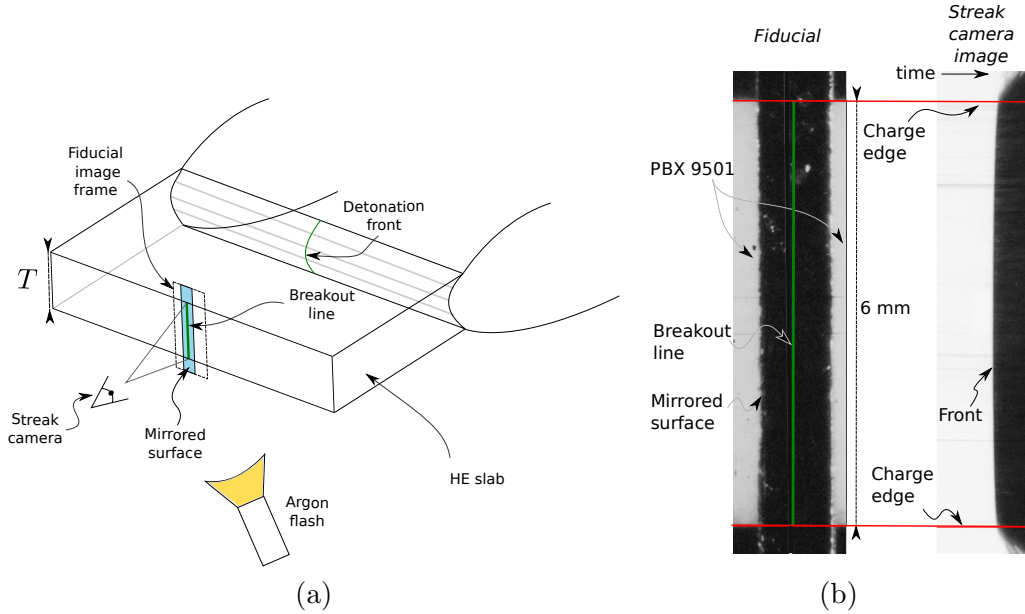
Figure 5: (a) Schematic diagram showing the mirrored detonation breakout surface and streak camera position. (b) Streak camera image of the detonation front breakout for the 6 mm thick charge, along with a fiducial image showing the explosive slab and attached mirror.
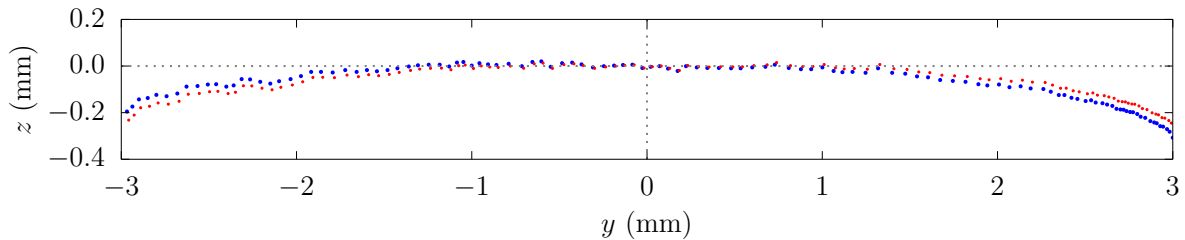

Figure 6: The original detonation front shape shown in • and its tilt-corrected analogue in • for the $T = 6.00$ mm test. The coordinate y measures the distance from the centerline along the short-axis direction of each test (Fig. 3).

(left)).

The front breakout records were manually sampled for discrete pixel locations on the streak camera image associated with the change in mirror surface reflectivity. With knowledge of the detonation phase speed for each test, the sampled wave's local breakout time can be transformed to a distance, yielding the detonation wave surface shape in physical space. Figure 6 shows the front surface shape $z(y)$ for the 6.00 mm charge test as function of the coordinate distance from the centerline y (Fig. 3). The front is positioned such that z(y=0)=0. The small asymmetry (tilt) with respect to the charge center $(y = 0)$ has various potential sources including the streak camera film placement and variations in the spin mechanism of the camera. Linear tilt corrections can be employed to correct for this variation, producing front data with comparable scatter with respect to a mean symmetric curve ([41, 42]). To evaluate this tilt correction, the following function [42]

Test	Width	a_1	a_2	η	ϕ_b	$(\Delta z)_{SE}$	$|A_y|$
#	(mm)	(mm)	(mm)		(deg)	(mm)	
8-1735	8.01	0.0938	——	0.9624	30.93	0.0079	0.028
8-1723	6.00	0.0998	——	0.9475	30.89	0.0096	0.012
8-1694	3.99	0.0985	0.0040	0.9334	29.40	0.0080	0.093
8-1691	3.00	0.1197	0.0117	0.9259	29.86	0.0162	0.112
8-1701	1.98	0.0882	——	0.8675	29.91	0.0182	0.222
8-1705	1.00	0.1117	——	0.7866	38.41	0.0095	0.057

Table 2: Log-form fit parameters. For 8-1735, 8-1723, 8-1701 and 8-1705, $n = 1$, while for tests 8-1691 and 8-1694, $n = 2$ in order to obtain a similar level of fit error $(\Delta z)_{SE}$ for all tests.

was used to fit each front shape,

$$z(y) = \sum_{i=1}^{n} a_i \left[\ln \left(\cos \left(\frac{\pi \eta}{T} y \right) \right) \right]^i + A_y y, \tag{1}$$

where the parameters a_i and η are fitting constants such that $0 < \eta < 1$, n is the number of terms used in the fit and A_y provides the linear tilt correction to the front shape digitization. The result of the least-squares optimization of a_i, A_y and η appear in table 2. There are a range of tilt magnitudes represented by $|A_y| = 0.012 - 0.222$, with one outlier (test # 8-1701). Figure 6 also shows the tilt-corrected front shape for the 6 mm slab case, obtained by subtracting the asymmetric contribution $A_y y$ from the original front shape record. The tilt-corrected experimental data for $y < 0$ is then reflected in the $y = 0$ axis, producing a complete detonation front shape record in the range $0 \leq y \leq 3$ mm. This procedure is carried out for all tests for which detonation front shape records are available.

Figure 7a compares the digitized tilt-corrected front shapes to the log-form fitted curves (1) for all the imaged slab cases. Figure 7b shows the fit error residuals on a normalized axis. It shows an even distribution of variation from the mean across each charge thickness. The standard errors $((\Delta z)_{SE})$ that appear in table 2 were calculated as

$$(\Delta z)_{SE} = \sqrt{\frac{1}{N_y} \sum_{i=1}^{N_y} \Delta z_i^2}, \tag{2}$$

where Δz_i is the i-th difference between the fitted curve and the experimental data points, and N_y is the number of sampled points. Standard errors range between $0.0079 - 0.0182$ mm.

The characteristic size of the scatter relative to the mean front shape in Fig. 7, as determined from the residuals of the log-form fits, is around 11.2 μm in standard error, but around 40 μm in terms of the amplitude of the variations. In comparison, the characteristic length scale of HMX grain diameters for pressed PBX 9501 has a peak (6% by volume) near 147 μm with a smaller counterpart at around 20 μm (Fig. 2b). The observed scatter is therefore characteristic of the heterogeneous grain structure of PBX 9501, in which the detonation will simultaneously pass over neighboring regions of HMX crystals and binder materials along the breakout surface (Fig. 2a).
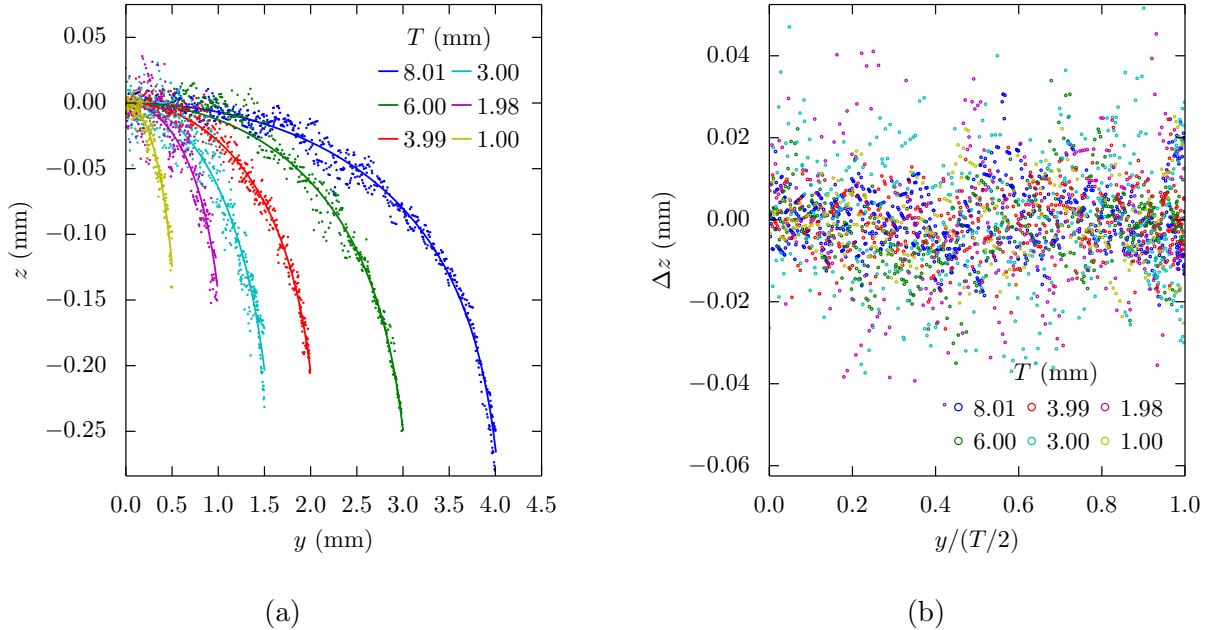
Figure 7: (a) Front shapes obtained from the slab tests (dots) along with the log-form fits (solid lines). (b) Fit error plotted with distance from the center, scaled with the half-charge thickness. In (a) and (b), the tilt-corrected experimental data to the left of $y = 0$ has been reflected across the centerline and combined with the corresponding data on the right-hand side of $y = 0$.

2.2. Parametric $D_n - \kappa$ data

In addition to providing a measure of experimental tilt and scatter, the log-form fits (1) also provide a measure of the mean detonation shock curvature (κ) and normal speed (D_n). Given a steady axial velocity D_0 and front shape $z(y)$, D_n and κ can are calculated from

$$D_n = \frac{D_0}{\sqrt{1 + (z')^2}}, \quad \kappa = -\frac{z''}{[1 + (z')^2]^{3/2}}, \tag{3}$$

where $z' = dz/dy$, $z'' = d^2z/dy^2$. The log-form fit function (1) for $z(y)$ yields smooth variations of the first and second derivatives ($z'(y)$ and $z''(y)$). The resulting D_n and κ variation for each slab case as a function of distance from the center of the slab scaled with the charge half-thickness is shown in Fig. 8. It is apparent that the most rapid variations in D_n and κ occur in a boundary layer near the charge edge, except for the thinnest slab ($T = 1.00$ mm), which shows a broad variation in curvature across the charge width. Parametrically plotting D_n versus κ shows the $D_n-\kappa$ relationship derived from each test (Fig. 9). The individual $D_n - \kappa$ curves are closely grouped for most of the range in curvature, diverging toward the edge of the charge. An underlying property for the suitability of the DSD model for a given explosive is that the $D_n - \kappa$ data for each front shape should group close to a single curve [43].

2.3. Calculated edge angles

The angle $\phi = \phi_b$ between the normal to the detonation shock surface at the edge of the explosive charge and the axial propagation direction is an important quantity in DSD theory. It is
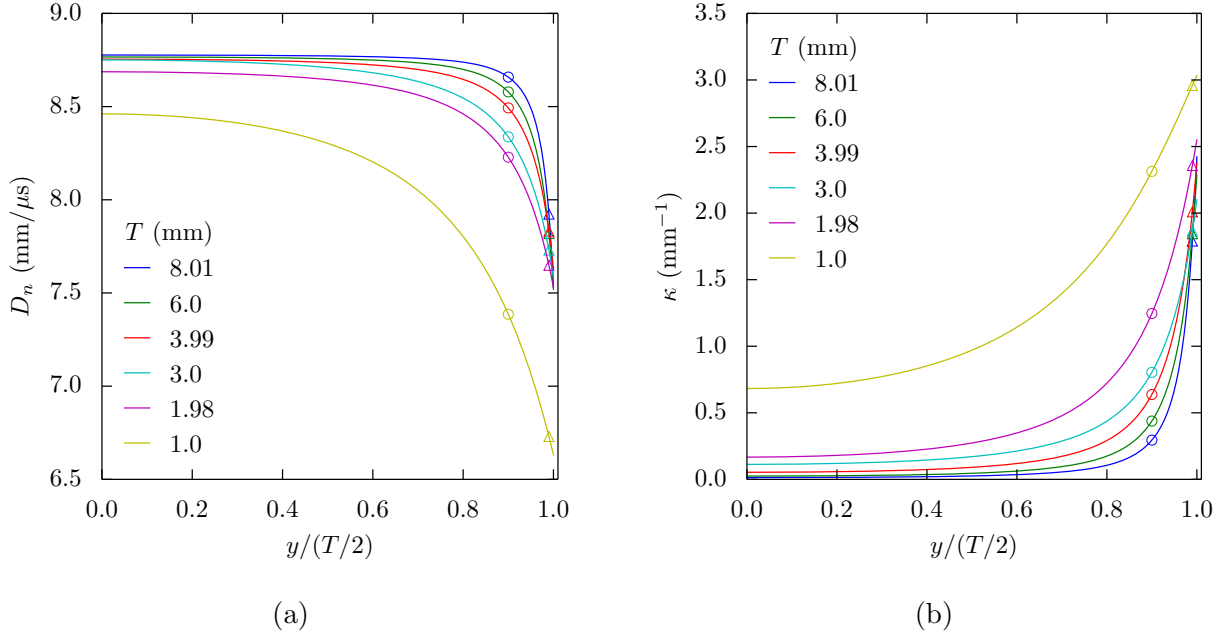
9

Figure 8: (a) Normal speed D_n and (b) curvature κ as a function of the distance from the charge center normalized by T/2. Data within the outer 10% and 1% of each front shape are indicated by an open circle placed at $y = 0.9(T/2)$ and an open triangle placed at $y = 0.99(T/2)$, respectively.

used as a boundary condition, setting the degree of confinement felt by the detonation wave in the HE, and therefore affecting the surface speed and shape in the DSD calculations. For the present calibration experiments, the HE slab charges were unconfined. Therefore, in a frame riding with the HE detonation shock at the HE charge edge, the flow immediately behind the detonation shock should be sonic at the HE charge edge [44]. For the slab experiments, the fitted log-form curves also provide an estimate for the sonic flow edge angle ($\phi_b = \phi_s$),

$$\phi_s = \tan^{-1}(dz/dy)|_{y=T/2}. \tag{4}$$

These range between $29.40°$–$38.41°$ across the various tests (see table 2). Note that without the smallest test ($T = 1.00$ mm with $\phi_b = 38.41°$), the range is considerably smaller, i.e. $29.40°$–$30.93°$.

3. Two-dimensionality of the centerline flow

As noted in §2, the slab geometry experiments are designed to produce a region of steady 2D planar flow along the centerline of the charge (Fig. 3). The angle at which the 3D flow region moves toward the slab centerline can be estimated by previous experiments measuring the penetration distance of waves originating at the unconfined surface of an HE. For example, for Composition B and PBX 9502, the penetration angles were estimated to be $14°$ [45], and $15°$ [46], respectively. In order to ensure a 2D planar flow region is established in the PBX 9501 slab geometry, a long-axis front shape measurement was taken for a 3 mm thick slab (test 8-1595, table 1). The long-axis measurement line is indicated schematically in Fig. 3 by the blue line. The front shape was sampled from the breakout streak image in a similar fashion to that described in §2.1. The result appears
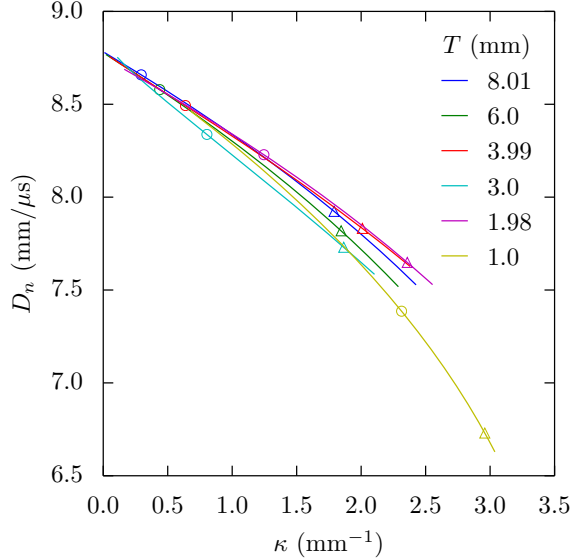
10

Figure 9: The D_n vs. κ variation for each slab case.

in Fig. 10a and shows a clear change in surface height amplitude as one moves from the long-axis charge edge into the interior, with a total deflection of around 0.4 mm relative to $z = 0$. The asymmetry observed in the surface heights between the two edge regions is conjectured to be due to variations in the linewave initiation dynamics at the charge edges. Figure 10b shows a bounded stochastic variation in surface height from $z = 0$ of size ≈ 40 μm for a section of the front near the charge center (of length ≈ 40 mm), indicating the existence of a 2D planar flow region near the charge center. If we assume the 2D flow region to be (at least) contained within $w \in [-20, 20]$ mm, based on the charge length of 135 mm, the penetration angle of the 3D flow region is $\approx 22°$.

The heterogeneous grain structure of PBX 9501 makes some variation likely in the measurement of the detonation front shape. If these observed variations are indeed due to heterogenity, we might expect that the variations in front shape around $z = 0$ observed in the central 2D flow region of the long-axis test will be comparable to those observed in the short-axis cases (§2.1). Figure 11 compares the measured deviations from $z = 0$ for the long-axis front shape (folded across the centerline) in the region -20 mm $< w < 20$ mm to the short-axis mean wave shape variations calculated in §2.1. Figure 11a shows this scatter as a function of a normalized distance axis. The maximal deviation magnitudes are similar. Statistically, the standard error value was 0.0152 mm for a distance of 20 mm from the center for the long-axis case, with an overall mean of 0.002 mm. For comparison, the standard error values for the short-axis cases ranged between 0.095–0.0182 mm for individual tests (see table 2), whereas the combined standard error across all the data sets was 0.0112 mm with a mean of -0.0005 mm. In Fig. 11b, histograms compare the distribution of the deviations from the mean between the long-axis and (combined) short-axis tests. The two distributions were clustered near zero with the vertical lines indicating the standard deviation values. Thus the variations from the mean surface shapes for the long- and short axis cases are comparable, pointing toward the PBX 9501 heterogeneous grain structure as the origin of the surface roughness.
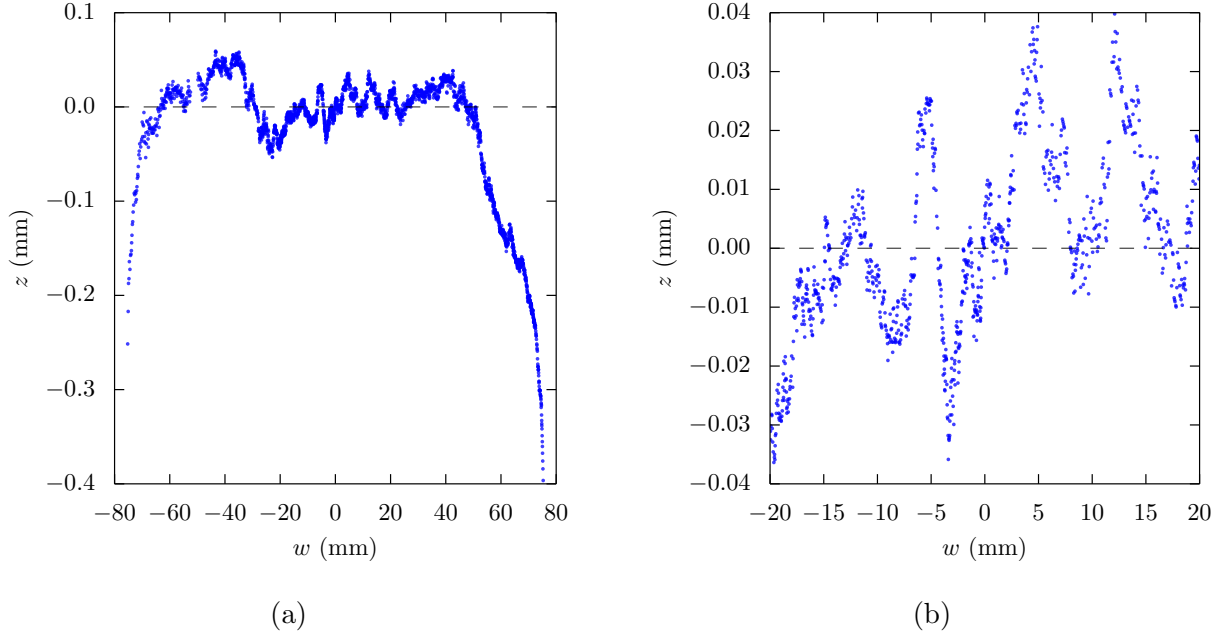
(a)   (b)

Figure 10: (a) Sampled front shape variation with long-axis coordinate (w) for the PBX 9501 ($T = 3.00$ mm) long-axis test. (b) Detail of the central region for $w \in (-20, 20)$ mm.
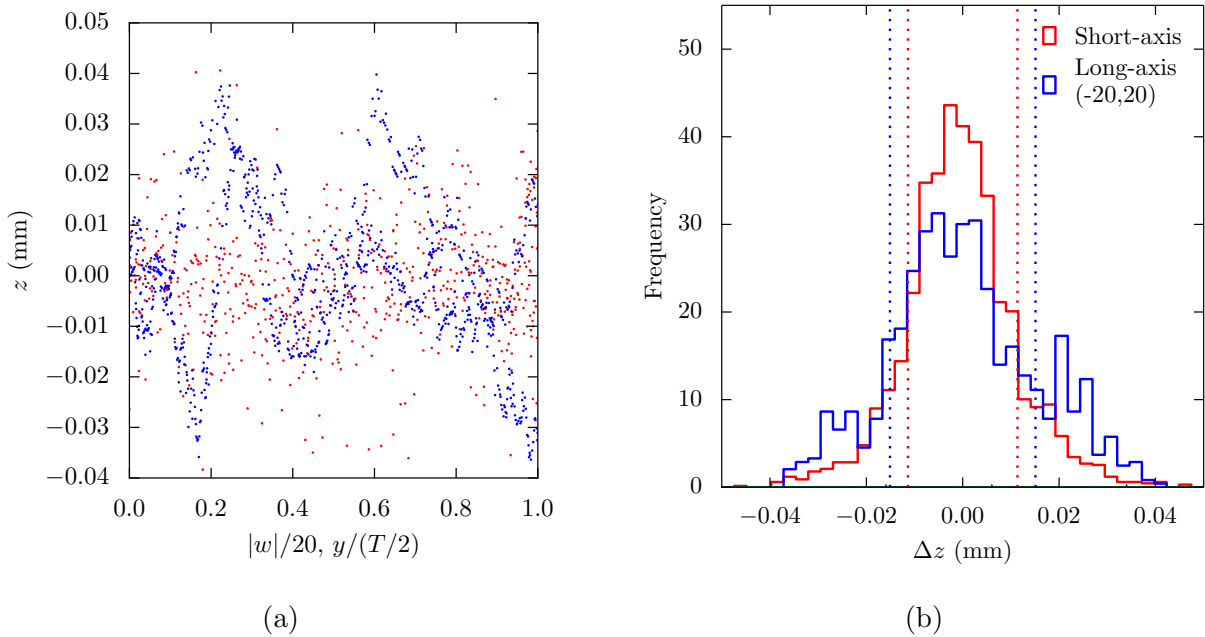

(a)   (b)

Figure 11: (a) The scatter from $z = 0$ for the region $w \in [-20.0, 20.0]$ for the long-axis front shape record (blue dots) and the scatter between all the short-axis front shapes and their respective log-form fits (red dots). (b) Histogram of the scatter showing similar distributions and standard deviations (indicated by the vertical lines) for the long- (——) and short-axis (——) cases respectively.
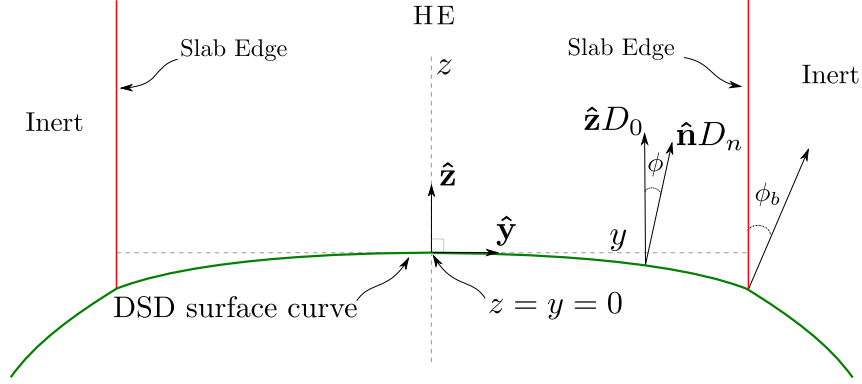
12

Figure 12: The 2D planar slab coordinate system and geometry for the DSD calibration.

4. DSD calibration

4.1. 2D Planar Slab Geometry DSD equations

To calibrate a specific $D_n(\kappa)$ function to the PBX 9501 thickness effect and front shape data shown in tables 1 and 2, the surface curvature is first related to a coordinate system representing the steady-state propagating DSD surface. Figure 12 shows the relevant slab geometry coordinate system, where, as in §2, y is distance from the slab centerline, z is the surface deflection, while ϕ represents the angle between the axial propagation direction and the normal to the DSD surface at any point on the surface. The resulting ordinary differential equations describing the steady DSD surface shape can be written as a function of either y or ϕ through geometrical arguments as

$$\frac{dz}{dy} = -\tan\phi, \quad \frac{d\phi}{dy} = \frac{\kappa_s}{\cos\phi}; \quad \frac{dz}{d\phi} = -\frac{\sin\phi}{\kappa_s}, \quad \frac{dy}{d\phi} = \frac{\cos\phi}{\kappa_s}; \tag{5}$$

where $\kappa_s = d\phi/d\xi$, and ξ is the arc length coordinate on the surface. For the 2D slab geometry, the total surface curvature $\kappa = \kappa_s$. The normal surface speed is

$$D_n = D_n(\kappa) = D_0 \cos\phi, \tag{6}$$

where D_0 is the steady axial propagation speed. Front shape symmetry is imposed at the slab centerline $y = 0$, i.e.

$$z(y = 0) = 0, \quad \phi(y = 0) = 0, \tag{7}$$

while at the charge edge the surface angle ϕ is set to ϕ_b,

$$\phi(y = T/2) = \phi_b. \tag{8}$$

The $D_n - \kappa$ propagation law we adopt is given by [47]

$$\frac{D_n}{D_{CJ}} = \left(1 - \alpha_1\kappa \frac{1 + \alpha_2\kappa + \alpha_3\kappa^2}{1 + \alpha_4\kappa + \alpha_5\kappa^2}\right), \tag{9}$$

13

where α_1, α_2, α_3, α_4, and α_5 are constant parameters to be calibrated. The Chapman-Jouguet speed D_{CJ} and surface edge angle ϕ_b are also not specified at this point.

The experimental slab thickness was considered a fixed quantity for comparing and fitting the DSD calculations to data. Consequently, a method was required for calculating D_0 given the charge thickness (T^{exp}), D_{CJ}, ϕ_b, and the DSD calibration parameters ($\alpha_1, \alpha_2, \ldots \alpha_5$), wherein we define the charge thickness as a function of $D_0 = D_0^{DSD}$ via integration of (5),

$$T(D_0) = 2 \int_0^{\phi_e} \frac{dy}{d\phi} d\phi = 2 \int_0^{\phi_e} \frac{\cos\phi}{\kappa_s} d\phi, \tag{10}$$

and iterate on D_0 until $T(D_0^{DSD}) = T^{exp}$. Additionally, a method was required for comparing the predicted DSD front shapes to the experimentally measured front shapes, where the experimental data are given as measurements of the surface shape height ($\mathbf{z}^{exp}$) with distance from the center ($\mathbf{y}^{exp}$) in vector form. In the following, the components of these vectors are denoted with subscripts, i.e. $\mathbf{y}_j^{exp}$, $\mathbf{z}_j^{exp}$ for $j = 1, \ldots, N_y$, where N_y is the number of sampled points in the experimental record. The corresponding DSD surface shape height ($\mathbf{z}_j^{DSD}$) is then calculated at each experimental coordinate $\mathbf{y}_j^{exp}$ via

$$\mathbf{z}_j^{DSD} = \int_0^{\mathbf{y}_j^{exp}} \frac{dz}{dy} dy, \tag{11}$$

where dz/dy is given by (5), and evaluated using the specified $D_n(\kappa)$ relation with D_0 calculated in (10) for a given T^{exp}, D_{CJ} and ϕ_b.

4.2. Merit function

With regard to the optimization of the parameters D_{CJ} and ϕ_b, we have two choices. First, they could be explicitly included in the DSD parameter optimization method described below along with the parameters α_i. However, with no constraints, our experience with this approach is that in driving the optimization to one with the lowest fitting error, often D_{CJ} and ϕ_b are driven to unphysically low or high values. Consequently, our approach is to fix both D_{CJ} and ϕ_b, optimize the DSD model fit based only on the α_i parameters, and then subsequently explore the variation of fits with both D_{CJ} and ϕ_b changed discretely within a range centered on experimentally informed knowledge of D_{CJ} and ϕ_b. The solution with the least fitting error is then selected within the range of D_{CJ} and ϕ_b explored. In order to quantify the fit quality of a particular DSD calculated set of surface shapes and speeds to the experimental data, a merit function was defined that incorporates both the error in the DSD calculated detonation thickness effect curve and the front shapes. It is given by

$$\mathcal{M} = w_{TE} \sum_{i=1,N_{TE}} \frac{1}{N_{TE}} \left(F_i(D_{0,i}^{DSD} - D_{0,i}^{exp}) \right)^2 + w_{FS} \sum_{i=1,N_{FS}} \sum_{j=1,N_t^i} \frac{1}{N_t^T} \left(E_i(\mathbf{z}_j^{i,DSD} - \mathbf{z}_j^{i,exp}) \right)^2, \tag{12}$$

where $\mathbf{z}_j^{i,DSD}$ and $\mathbf{z}_j^{i,exp}$ represent the DSD calculated and experimental j-th surface shape z-coordinate for the i-th test respectively, $D_{0,i}^{DSD}$ and $D_{0,i}^{exp}$ are the DSD calculated and experimental detonation speed for the i-th test respectively, $N_{TE} = 8$ (the number of thickness effect points), N_t^i is the number of surface shape coordinates for the i-th test, $N_t^T = \sum_{i=1..N_{FS}} N_t^i = 2597$ is the

D_{CJ} (mm/μs)	α_1 (mm)	α_2 (mm)	α_3 (mm^2)	α_4 (mm)	α_5 (mm^2)	ϕ_b (radians)
8.79	0.049654	0.059285	0.158482	0.005573	6.57673×10^{-5}	$\pi/6$

Table 3: DSD slab geometry calibrated $D_n - \kappa$ parameters for PBX 9501.

total number of front shape coordinate points across all tests and $N_{FS} = 6$ (the number of tests for which front shape data was obtained). The merit function definition in (12) is based on the approach of Bdzil *et al.* [47] and is constructed with separate thickness effect and surface shape error component sums. The factors E_i and F_i serve to weight the contribution of each error to the merit function and were defined as

$$F_i = (\mathbf{f})_i/D_{0,i}^{exp}, E_i = 1/(T_i^{exp}/2) \tag{13}$$

where T_i^{exp} was the charge-thickness for the i-th test and $\mathbf{f}$ is an additional weight vector for the thickness effect data. It was defined such that the multiple tests at $T = 3$ mm were given equivalent weights of $1/3$ to avoid bias in the fit to that specific charge thickness calculation, i.e.

$$\mathbf{f} = \begin{pmatrix} 1 & 1 & 1 & 1/3 & 1/3 & 1/3 & 1 & 1 \end{pmatrix}^T. \tag{14}$$

The relative contribution between the two sets of errors is largely determined by w_{TE} and w_{FS}. In the calibrations described below, $w_{FS} = 0.256$ and $w_{TE} = 1.0$, again a choice based on experience of the authors with the DSD model calibration technique across a range of explosives. It ensures that fitting of the front shape data plays a significant role in the calibration of the $D_n - \kappa$ model. Finally, the optimized parameters of the $D_n - \kappa$ relation were obtained by numerically minimizing the multivariable merit function via a Levenberg-Marquardt least-squares algorithm [48]. Given the inherent flexibility in the merit function parameter choices, it is essential that validation tests be conducted on any derived PBX 9501 $D_n - \kappa$ model, as conducted in [23].

4.3. DSD Model for PBX 9501

Following the procedure described in §4.1 and 4.2, the resulting $D_n - \kappa$ calibration parameters are shown in table 3. The explicit $D_n - \kappa$ variation is shown in Fig. 13. Figure 14a shows the DSD thickness effect variation resulting from the calibration to slab geometry experiments. The difference between the DSD model and experimental speed for each slab thickness is shown in Fig. 14b, where the DSD fit has a standard deviation error of 7.5 m/s relative to the experimental data (in comparison, for the three tests performed at $T = 3.0$ mm, the experimental speed measurements varied by 28 m/s from the lowest to highest speed). Figure 14c shows the calibrated DSD surface shapes and the corresponding experimental detonation front shapes. The standard error across all DSD front shapes was 0.015 mm (Fig. 14d).

Accurately detailing the uncertainty in the $D_n - \kappa$ model is complex. The log-form fitting-function derived D_n and κ variation for each specific slab case, as shown in Fig. 9, can provide some useful estimate of the uncertainty in our global DSD $D_n - \kappa$ model shown in Fig. 13. However, the log-form specification (1) does not possess the surface based propagation physics contained within the DSD $D_n - \kappa$ formulation. In order to address this, we can instead apply the DSD model parameterization approach described in §4.1 and §4.2 to each individual slab geometry case
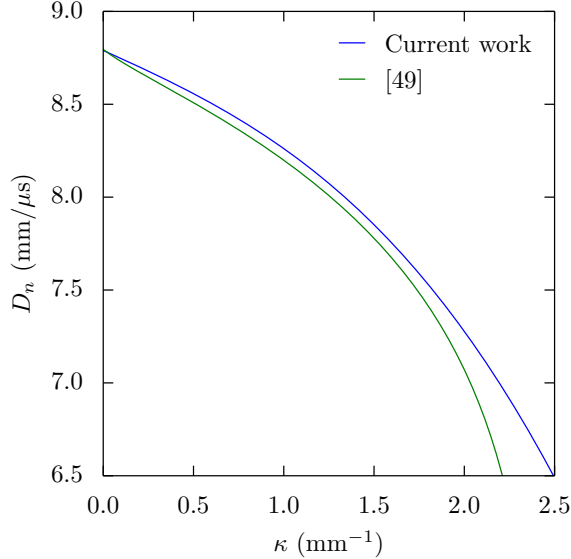
Figure 13: Variation of D_n with κ for the slab geometry calibrated DSD model for PBX 9501 (current work). Also shown is that derived in [49].

separately rather than globally, ensuring an appropriate balance between the errors in the axial detonation speed and front shape. Effectively, we derive a separate $D_n - \kappa$ relation for each slab case to estimate model uncertainty. These curves are shown in Fig. 15 along with the global or base DSD $D_n - \kappa$ relation. For small to moderate curvatures, the individual D_n variations for each slab case are tightly grouped, with the D_n variations increasing in magnitude as κ increases. At $\kappa = 2$ mm^{-1} (approximately the maximum curvature accessed in the slab DSD calculations), the two bounding curves for D_n for the $T = 3.00$ mm and $T = 8.01$ mm slabs deviate from the global DSD $D_n - \kappa$ relation by $O(100)$ m/s. While limited, the above analysis is indicative of the level of shot-to-shot uncertainty in the $D_n - \kappa$ behavior. That said, in §5, we show that the slab-geometry calibrated DSD relation (9), populated by the PBX 9501 parameters in table 3, gives excellent predictions of the detonation propagation behavior in PBX 9501 2D circular arc geometry validation tests.

### 4.3.1. Prediction of the rate-stick geometry diameter effect curve

The DSD model is a coordinate-free surface propagation concept. This implies that once a DSD model is parametrized using data solely from one geometry, it should be able to capture detonation motion in other geometries [26]. Figure 14a shows the diameter effect curve obtained from the slab-geometry calibrated DSD model compared with previously obtained experimental, unconfined, diameter effect data points [26]. The DSD prediction for the diameter effect curve overpredicts the experimental diameter effect data, with the difference growing as the rate-stick radius decreases (between data points at radii of $R = 2.505$ and $R = 1.415$ mm, the error grows from $O(15)$ to $O(50)$ m/s). With regard to the experimental data, we note that the thickness and diameter effect curves almost overlay when plotted as the variation of D_0 vs. $1/T$ or $1/R$ (Fig. 14a). In principle, this can only occur if the two components of curvature in the rate-stick geometry, i.e.
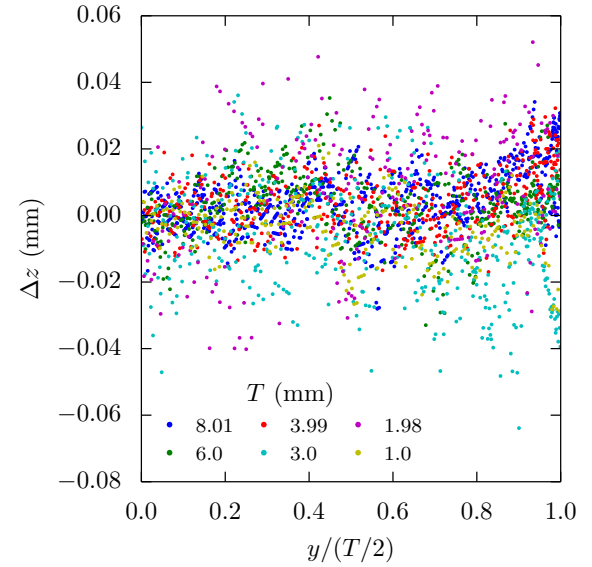
16
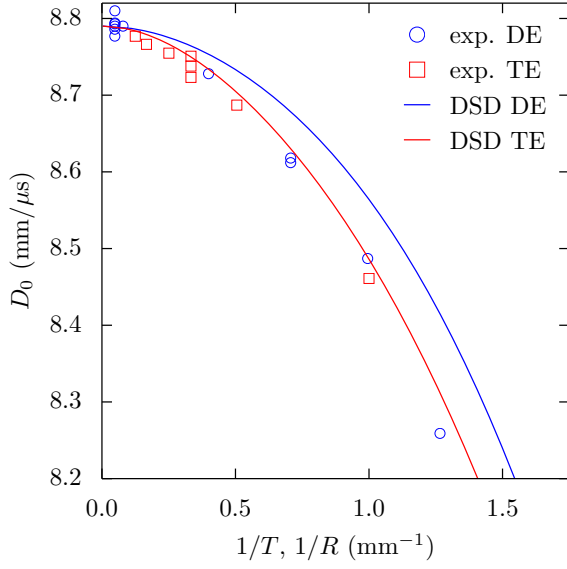
(a)
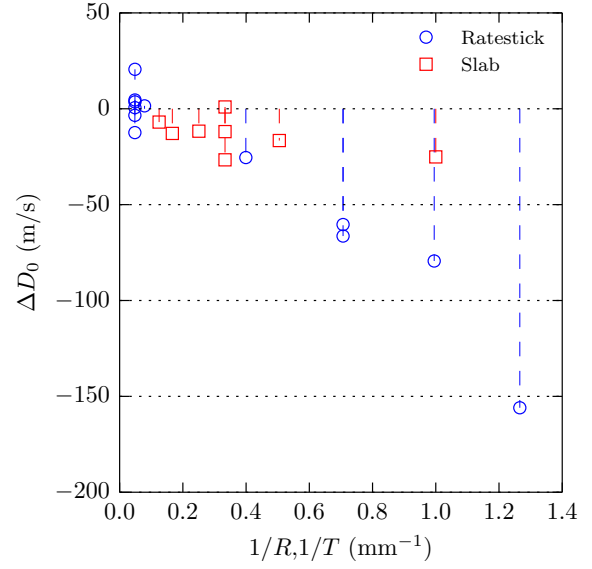
(b)
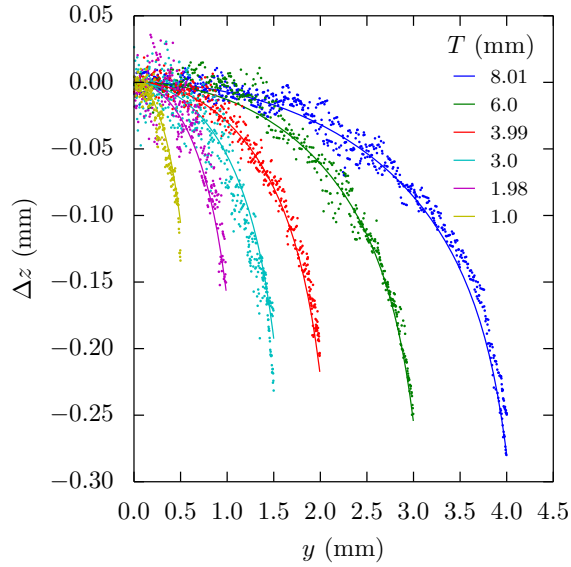
(c)

(d)

Figure 14: Results of the DSD model parameter fitting procedure for the relation (9) with PBX 9501 parameters shown in table 3. (a) Thickness effect variation (DSD TE) calibrated to slab geometry data (exp. TE). Also shown is the DSD predicted diameter effect curve (DSD DE) compared against rate-stick geometry experiments (exp. DE). (b) Difference between the slab geometry calibrated DSD model and experimental speed for each experimental slab thickness or rate stick radius. (c) Comparison between the DSD surface front shapes and slab geometry experiment detonation shock shapes, with relative differences shown in (d).
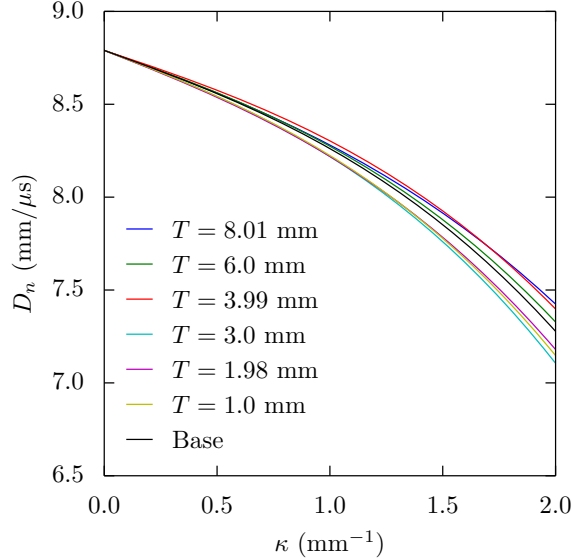
Figure 15: Variation of D_n with κ based on fitting the $D_n - \kappa$ relation (9) separately to each individual slab geometry case. Also shown is the global DSD $D_n - \kappa$ relation (9), populated by the PBX 9501 parameters in table 3 (Base).

the slab and axisymmetric components, were equal, i.e. the front was a spherical cap [24, 26]. This would correspond to a detonation with an infinitely thin reaction zone. However, Jackson & Short [26] showed that the axisymmetric component of curvature in a rate-stick geometry must be less than the slab component at each point across the charge. Thus, when the detonation speed data are plotted against $1/T$ and $1/R$ for the slab and rate stick geometry respectively, the diameter effect curve must lie above that of the thickness effect curve, as demonstrated by the DSD model behavior.

This points to a potential inconsistency in the make-up of the PBX 9501 explosive used for the slab and rate-stick tests. We note that the rate-stick test data was obtained approximately 20 years prior to the slab geometry data mostly using a different lot of PBX 9501 molding powder [26]. Also, for the rate stick data, two shots with the same radius 20.65 mm and with the same reported density (1.838 g cm^{-3}) show a speed difference of 17 m/s [26]. This data gives some indication of the inherent experimental variability in speed measurements. However, the data is too sparse to be used to provide a statistically relevant analysis. In contrast, as noted above, in §5 we show that the slab-geometry calibrated DSD relation gives excellent predictions of the detonation propagation behavior in PBX 9501 2D circular arc geometries, experiments that used the same lot of PBX 9501 molding powder and pressed to a similar density as the current slab tests. Nevertheless, the DSD approximation for the rate-stick geometry is significantly improved over a Huygens approximation, where, for example, for $R = 1.415$ mm the difference between the experimental detonation propagation speed and a Huygens approximation is 178 m/s, while for $R = 1.005$ mm, it is 303 m/s.

A $D_n(\kappa)$ relation for PBX 9501 based solely on rate-stick cylindrical geometry experiments has

D_{CJ} (mm/μs)	α_1 (mm)	α_2 (mm)	α_3 (mm^2)	α_4 (mm)	α_5 (mm^2)	A (mm^{e_1})	D_1 (mm^{-1})	e_1	ϕ_b (rad.)
8.795	0.03655	0.05693	0	4.313	0	1.406	2.443	0.0778	0.6301

Table 4: DSD rate stick-geometry calibrated $D_n - \kappa$ parameters [49].

been derived previously [49] using the $D_n - \kappa$ functional form,

$$\frac{D_n}{D_{CJ}} = \left(1 + A((D_1 - \kappa)^{e_1} - D_1^{e_1}) - \alpha_1\kappa \frac{1 + \alpha_2\kappa + \alpha_3\kappa^2}{1 + \alpha_4\kappa + \alpha_5\kappa^2}\right). \tag{15}$$

The parameters of this $D_n - \kappa$ calibration appear in Table 4. Although this $D_n - \kappa$ relation fits the rate stick diameter effect data well since it is calibrated to that data (Fig. 16a), the more rapid decrease of D_n with κ seen in Fig. 13, based on the relation (15), results in smaller phase velocities in the slab geometry than observed experimentally. Significantly, the associated DSD surface shapes poorly capture the slab geometry detonation shock shapes (Fig. 16b), generally possessing too much curvature across the charge width. We demonstrate below that the PBX 9501 DSD relation [49] also does not effectively predict the 2D circular arc geometry detonation propagation behavior. Yet another PBX 9501 $D_n - \kappa$ model form was used for so-called wave passover validation experiments as described in [17]. However, the parameters for the PBX 9501 DSD model used in [17] were not explicitly stated, and therefore could not be compared with our current results.

5. Application to the Two-Dimensional PBX 9501 Circular Arc Geometry

For use in engineering problems, the DSD propagation law (9), populated by the PBX 9501 parameters in table 3, is combined with a surface evolution construction. Assuming a set of level curves given by $f(\mathbf{x}(t), t) = c$, where c is a constant, with the unit normal to each surface given by $\mathbf{n} = \nabla f/|\nabla f|$, the level set evolution equation can then be written as

$$\frac{\partial f}{\partial t} + D_n|\nabla f| = 0, \quad D_n = \mathbf{n} \cdot \frac{d\mathbf{x}}{dt}, \tag{16}$$

where $D_n(\mathbf{x}, t)$ is the surface normal speed and related to curvature κ by

$$D_n = D_n(\kappa), \quad \kappa = \nabla \cdot \mathbf{n}, \tag{17}$$

where κ is the total surface curvature. The zero level set represents the required evolution of the DSD surface motion.

In Short et al. [23], three validation experiments were described that explored some of the properties of PBX 9501 detonation in a two-dimensional circular arc geometry of varying thickness and inner radius. The circular arc configuration is the simplest geometry that accounts for modifications of the detonation front curvature induced by diffraction. The three PBX 9501 arc sections had dimensions: 65.35 mm (R_i) x 67.35 mm (R_e) x 200 mm (width); 65.47 mm (R_i) x 69.97 mm (R_e) x 200 mm (width); and 100.35 mm (R_i) x 120.35 mm (R_e) x 200 mm (width) [Fig. 17a]. Here R_i represents the interior (inner) radius dimension, while R_e is the exterior (outer) radius.
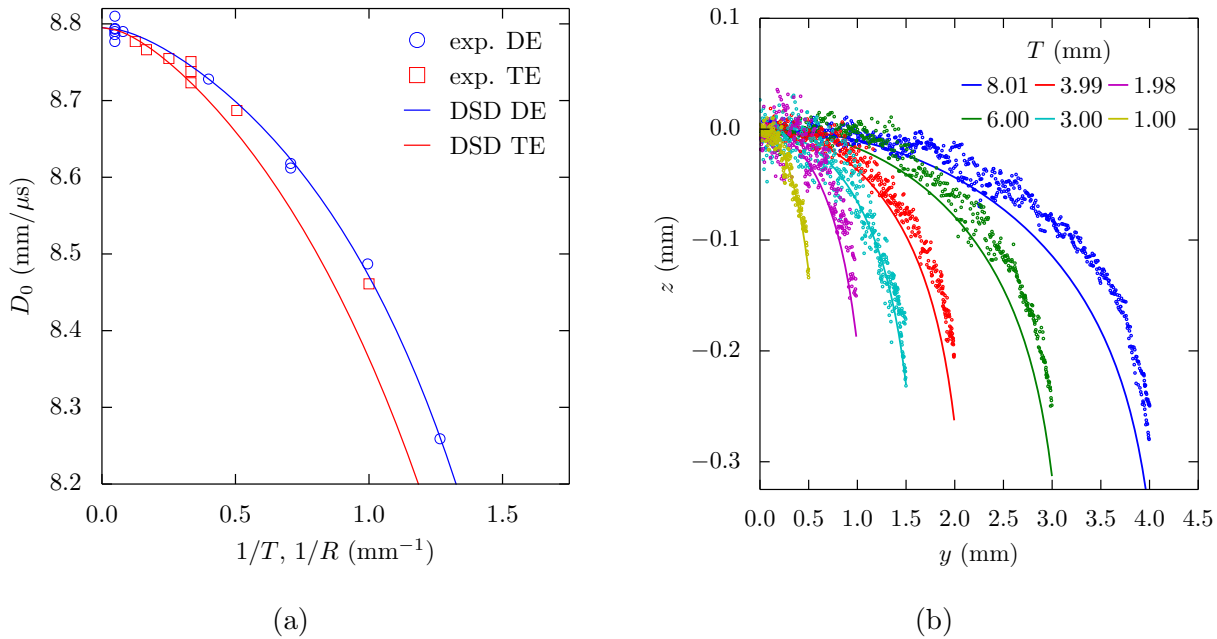
(a)

(b)

Figure 16: (a) Diameter effect variation (DSD DE) calibrated to rate-stick geometry data (exp. TE) from [49]. Also shown is the DSD predicted thickness effect curve (DSD TE) compared against slab geometry experiments (exp. TE). (b) Prediction of the slab geometry surface front shapes based on the rate-stick geometry calibrated DSD model with with slab geometry experiment detonation shock shapes.
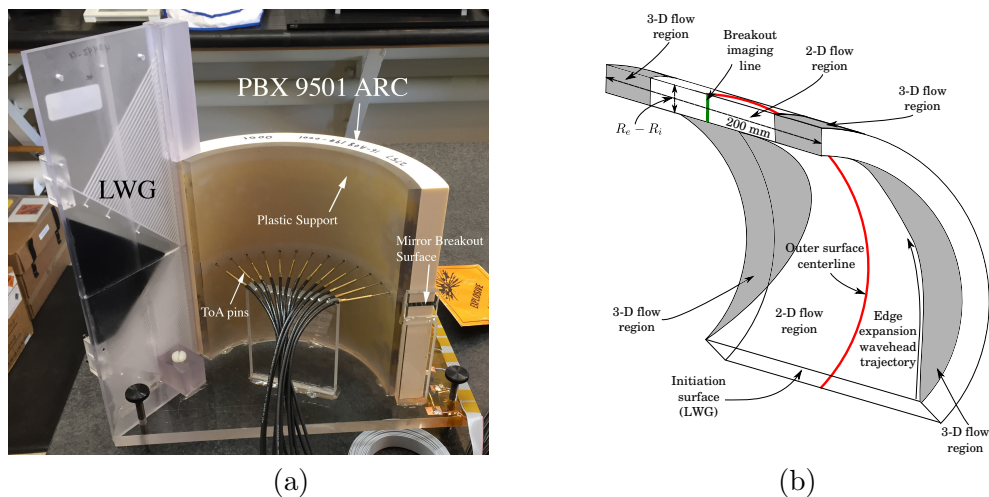

(a)

(b)

Figure 17: (a) Image of the 100.35 x 120.35 x 200 mm PBX 9501 arc test. (b) Schematic illustrating how the flow along the inner and outer surface centerlines remains two-dimensional for the arc section. Both images are taken from [23].

The angular extent of each of the arc sections was $\approx 3\pi/4$ radians. The large (200 mm) width of the arc sections ensured that the flow along the arc centerline remained two-dimensional, as shown schematically in Fig. 17b and described in [23], in a similar manner to that for the slab geometry experiments (§2). The detonation is initiated uniformly along the width of each arc section with a line wave generator (LWG) placed in direct contact with the PBX 9501 arc [23] (see Fig. 17a). Time-of-arrival (ToA) diagnostics were located along the centerline of both the inner and outer arc surfaces, and were used to determine the linear detonation speed on the inner and outer surface centerlines once the detonation wave had reached steady state propagation, and thereby rotating with a constant angular speed. The shape of the detonation surface at the end of the arc (Fig. 17a,b) was also measured as described in [23].

We now explore the physics of PBX 9501 detonation propagation for the circular arc geometry through the DSD model, including model validation based on the arc experiments [23], the effect of arc thickness, inner radius, relaxation dynamics to steady-state propagation and confinement effects. A polar coordinate (r, θ) representation of the evolution equation (16) specialized to the zero level set is employed, i.e. with $f = \theta - \theta_s(r, t) = 0$,

$$\theta_{s,t} = \frac{D_n}{r}(r^2\theta_{s,r}^2 + 1)^{\frac{1}{2}}, \quad \kappa = -\frac{r}{(r^2\theta_{s,r}^2 + 1)^{\frac{3}{2}}}\left(\theta_{s,rr} + \theta_{s,r}\left(r\theta_{s,r}^2 + \frac{2}{r}\right)\right), \tag{18}$$

where θ is the polar angle, r is the radial coordinate and $\theta_s(r, t)$ represents the motion of the DSD surface in the arc geometry under varying curvature. Note that the surface curvature κ can be split into two components,

$$\kappa = -\frac{(r\theta_{s,rr} + \theta_{s,r})}{(r^2\theta_{s,r}^2 + 1)^{\frac{3}{2}}} - \frac{\theta_{s,r}}{(r^2\theta_{s,r}^2 + 1)^{\frac{1}{2}}}, \tag{19}$$

where the first term on the right hand side represents the change in surface normal angle with surface arclength along the DSD surface, while the second term represents the rate-of-change of polar angle with arclength moving along the surface [21]. On the inner arc surface $r = R_i$,

$$\theta_{s,r} = -\frac{1}{R_i}\tan\phi_i, \tag{20}$$

while on the outer arc surface $r = R_e$,

$$\theta_{s,r} = -\frac{1}{R_e}\tan\phi_e, \quad \phi \leq \phi_s, \tag{21}$$

with a quadratic extrapolation condition for $\phi > \phi_s$. The latter mimics supersonic outflow that is observed in the reactive burn solutions, as detailed in [21, 39]. Here ϕ_i is the surface normal angle on the inner arc boundary, while ϕ_e is that on the outer arc boundary. For all the configurations considered below, except for Fig. 22b, we consider unconfined arcs for which $\phi_i = -\phi_s$ and $\phi_e = \phi_s$, with $\phi_s = \pi/6$. Confinement effects with $\phi_e = -\phi_i < \phi_s$ are explored in Fig. 22b. Equations (18) are solved on a mesh $R_i \leq r \leq R_e$, with $0 \leq \max(\theta_s) \leq 3\pi/4$. Second order upwinding is used for the derivative $\theta_{s,r}$ and combined with central differencing for $\theta_{s,rr}$. Time integration is via a second-order Heun's method. At $t = 0$, the DSD surface $\theta_s(r, 0) = 0$ for $R_i \leq r \leq R_e$ is assigned a normal speed of $D_n = D_{CJ}$ and subsequently evolved in time. For the purposes of transitioning smoothly from the initial surface state where $\theta_{s,r} = 0$ on $r = R_i$ and $r = R_e$, we linearly increase

Table 5: Linear speeds of the steady detonation motion along the inner $(r = R_i)$ and outer $(r = R_e)$ arc surfaces for the 3 arc tests described in [23], showing a comparison between experimental (Exp.) measurements, a surface evolution simulation using (18)–(21) with the DSD model (9) populated by PBX 9501 parameters in table 3 (DSD), and with the DSD model from [49] (DSD [49]).

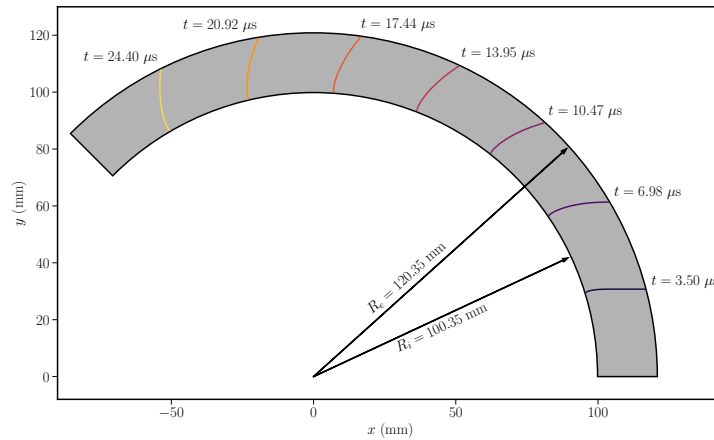| R_i-R_e (mm)	Speed (R_i) (mm μs^{-1})	Speed (R_i) (mm μs^{-1})	Speed (R_i) (mm μs^{-1})	Speed (R_e) (mm μs^{-1})	Speed (R_e) (mm μs^{-1})	Speed (R_e) (mm μs^{-1})
Exp.	Exp.	DSD	DSD [49]	Exp.	DSD	DSD [49]
65.35-67.35	8.582($\pm$0.013)	8.583	8.536	8.831($\pm$0.003)	8.846	8.797
65.47-69.97	–	8.593	8.558	9.186($\pm$0.006)	9.183	9.146
100.35-120.35	8.664($\pm$0.021)	8.640	8.612	10.411($\pm$0.018)	10.362	10.328

Figure 18: Evolution of the DSD surface in a circular arc with dimensions 100.35 mm (R_i) x 120.35 mm (R_e).

the surface angles on $r = R_i$ and $r = R_e$ from zero to ϕ_i or ϕ_e in time over a time period of 0.1 μs. Note that we can not provide absolute timing comparisons between the DSD calculations shown below and the experiments described in [23] as an experimental diagnostic to determine an absolute time-of-arrival of the detonation wave from the LWG at the initiating $(\theta = 0)$ PBX 9501 arc surface was not deployed.

Table 5 shows the linear speeds on the inner $(r = R_i)$ and outer $(r = R_e)$ arc surfaces for the unconfined arc geometries described in [23] (65.35 mm (R_i) x 67.35 mm (R_e); 65.47 mm (R_i) x 69.97 mm (R_e); and 100.35 mm (R_i) x 120.35 mm (R_e)) when $\max(\theta_s(r,t))$ equals $3\pi/4$, calculated using the above numerical formulation of (18)–(21) with the DSD model (9) populated by the newly calibrated PBX 9501 parameters in table 3. Here, $\phi_i = -\phi_s = -\pi/6$ and $\phi_e = \phi_s$, as the arcs are unconfined. For each arc geometry, there is a transient evolution, before the wave relaxes to a steady state propagation mode rotating with a constant angular speed, which we denote hereafter as ω_0 (radians/μs). Figure 18 shows an example of the motion of the PBX 9501 DSD surface for the unconfined 100.35 mm (R_i) x 120.35 mm (R_e) arc geometry, remapped to a Cartesian space. In each case, the DSD surface motion obtained from the time-dependent DSD formulation (18)–(21), after the surface had propagated through the range $0 \leq \max(\theta_s) \leq 3\pi/4$, is observed to be in steady-state. In fact, as further described below, in each arc case, the DSD surface wave relaxes to a steady state propagation mode significantly before the point where $\max(\theta_s) = 3\pi/4$.
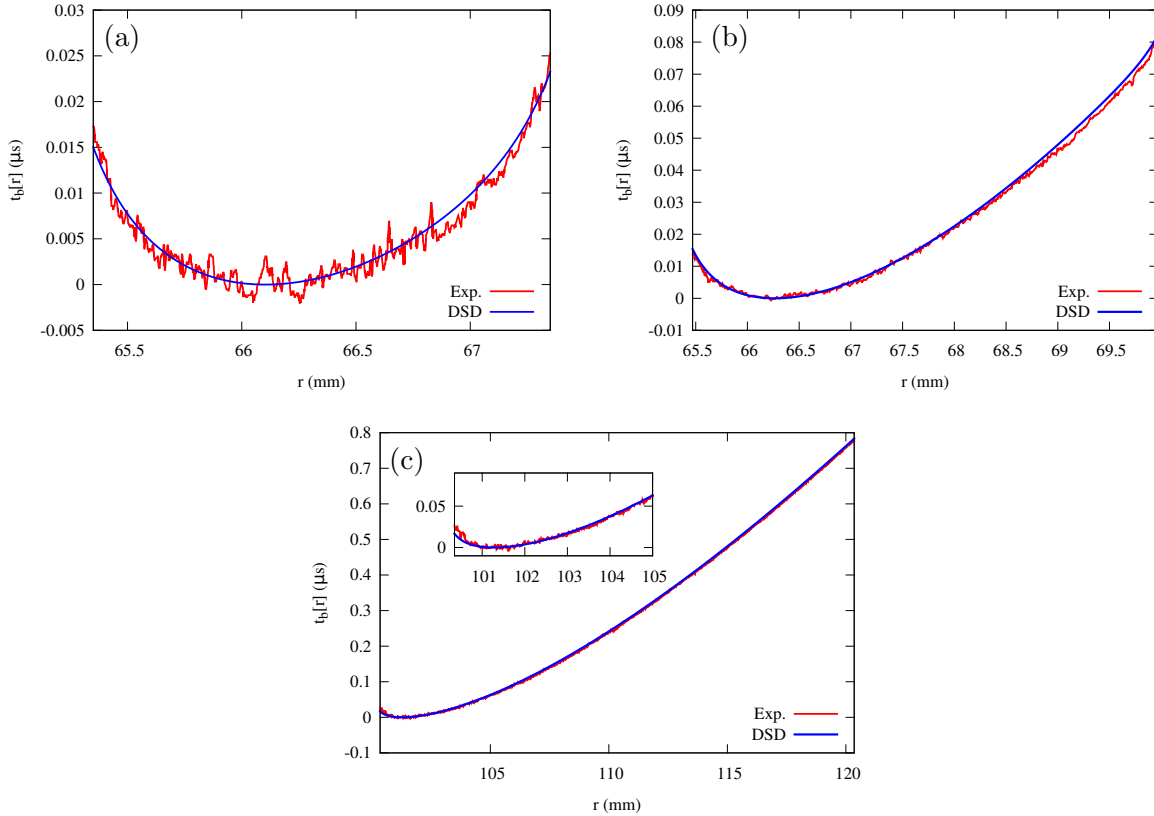
Figure 19: Relative breakout times t_b from the end of the arc surface for each point on the detonation shock as a function of radial coordinate for (a) 65.35 mm (R_i) x 67.35 mm (R_e), (b) 65.47 mm (R_i) x 69.97 mm (R_e) and (c) 100.35 mm (R_i) x 120.35 mm (R_e) arcs, comparing experimental results with the DSD model predictions.

As shown in table 5, the comparisons between our DSD model predictions and the experimental results for the linear speeds on $r = R_i$ and $r = R_e$ of the steady detonation motion are excellent. For the 65.35 mm x 67.35 mm and 65.47 mm x 69.97 mm arcs, the differences are at most 0.015 mm/μs or 15 m/s (note that for the inner arc surface on the 65.47 mm x 69.97 mm arc, a steady speed was not calculated due to the presence of jetting observed between the inner arc surface and a plastic support [23], which we hypothesized affected the ToA diagnostic triggering). For the 100.35 mm x 120.35 mm arc, the difference was observed to be 24 m/s on the inner surface and 49 m/s on the outer, representing errors of 0.28% and 0.47% respectively. For comparison, as described in [23], a Huygens model construction would have a steady wave speed of $D_{CJ} = 8.79$ mm/μs on the inner arc surface for all three arcs, and $R_e D_{CJ}/R_i = 9.059$, 9.394 and 10.542 mm/μs on the outer surfaces. Clearly, curvature effects are important even for a conventional high explosive like PBX 9501. We also note that the PBX 9501 DSD model from [49] has significantly higher errors than the present slab-geometry calibrated PBX 9501 DSD model. For the 65.35 mm x 67.35 mm and 65.47 mm x 69.97 mm arcs, the speed errors are in the range O$(30-50)$ m/s, with errors of 52 m/s on $r = R_i$ and 83 m/s on $r = R_e$ for the 100.35 mm x 120.35 mm arc (table 5). Figure 19 shows a comparison of the relative breakout time shapes from the arc end surface for the DSD model and the experiment for each arc geometry. The breakout shapes for the DSD calculations are obtained
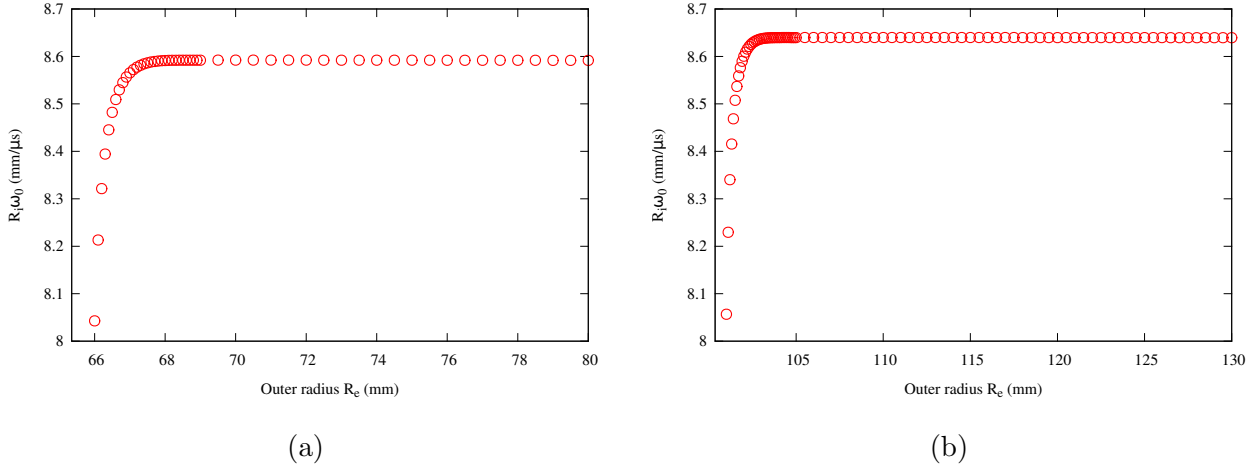
Figure 20: Variation of the steady linear speed $R_i\omega_0$ along the inner arc surface due to changes in the outer radius R_e for (a) $R_i = 65.35$ mm and (b) $R_i = 100.35$ mm. The circles represent the specific values of R_e for which the calculations were conducted.
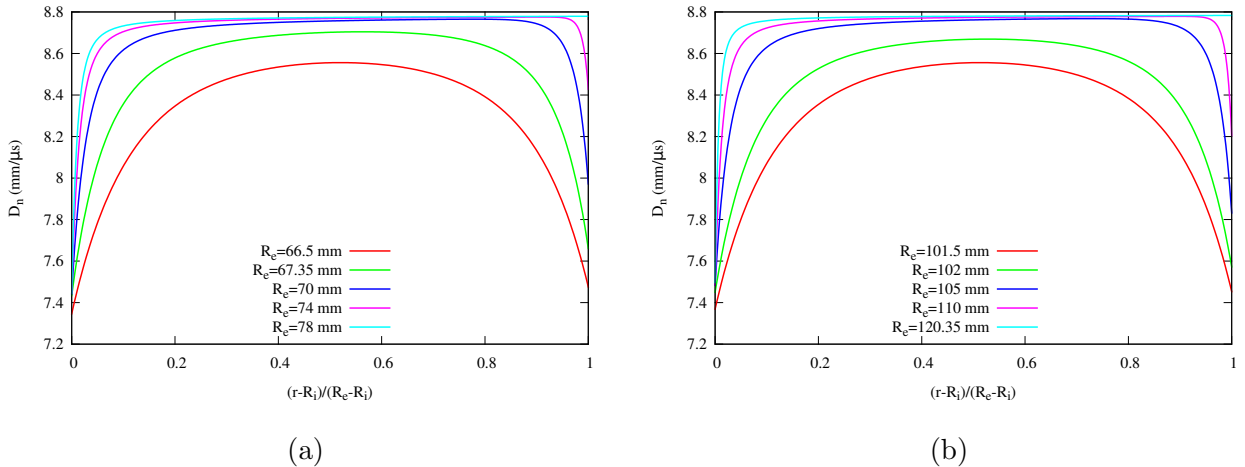

Figure 21: Variation of D_n across the DSD surface as a function of the scaled radial coordinate $(r - R_i)/(R_e - R_i)$ for (a) $R_i = 65.35$ mm and (b) $R_i = 100.35$ mm for several of the R_e values in Fig. 20, showing that the DSD surface senses the outer arc confinement (sonic) angle even after the angular speed has limited to a constant value.

through the relation $t_b(r, t) = (max[\theta_s(r, t)] - \theta_s(r, t))/\omega_0$ [23], recognizing that the motion is in steady-state at the breakout surface. In all cases, the agreement is again excellent.

5.1. Effect of varying arc thickness

It was shown in [21, 39, 40] that the scaled arc thickness $(R_e - R_i)/R_i$ has a complex influence on detonation propagation in the arc geometry. Figure 20a shows the linear detonation speed $R_i\omega_0$ of the DSD surface along $r = R_i$, at the time when $max(\theta_s) = 3\pi/4$, as a function of varying outer radius R_e for $R_i = 65.35$ mm and $R_i = 100.35$ mm (for all values of R_e shown, the surface propagation becomes steady significantly before the time when $max(\theta_s) = 3\pi/4$). For $R_i = 65.35$ mm, $R_i\omega_0$ limits to a constant when $R_e \gtrsim 68$ mm. Consequently, for an arc thickness larger than approximately 2.65 mm, the angular speed ω_0 at which the surface sweeps around the

24

arc, after reaching steady-state propagation, does not depend on the arc thickness. The surface structure, however, still senses the presence of the angle (sonic) confinement condition on $r = R_e$ until $R_e > 77.1$ mm, whereupon the extrapolation condition contained within (21) is engaged. This effect can be seen in Fig. 21a, which shows the variation of surface normal speed D_n across the DSD surface for several of the R_e values in Fig. 20a. For $R_e = 70$ and 74 mm, there is an adjustment layer in D_n near the outer arc boundary to meet the confinement (sonic) angle condition, even though ω_0 is almost identical in both cases. Only for $R_e > 77.1$ mm, does the (supersonic) extrapolation condition become active, as seen in Fig. 21a for $R_e = 78$ mm. The effect of having ω_0 the same while changes in the surface structure are observed for increasing R_e has been explained in [21]. For sufficiently wide arcs, ω_0 is determined by the surface curvature variations in a boundary layer attached to the inner arc surface, so that ω_0 depends on the inner arc radius R_i, confinement angle ϕ_i and the form of the $D_n(\kappa)$ variation defined by the DSD model. Outside of this inner arc boundary layer, the DSD surface propagates with D_n close to D_{CJ}, while a third layer is present near the outer arc surface to meet the confinement conditions on $r = R_e$ [21]. Neither of the two outer layers influence the determination of ω_0 to the order calculated. When the extrapolation conditions engage, the third layer is absent. For the present study, we are able to provide the above quantitative values on R_e for when these effects occur for PBX 9501 detonation.

For $R_i = 65.35$ mm and $R_e \lesssim 68$ mm, $R_i\omega_0$ decreases monotonically, with a progressively larger drop for decreasing R_e (Fig. 20a). For instance, $R_i\omega_0 = 8.043$ mm/μs for $R_e = 66.0$ mm, while for $R_e = 65.9$ mm, $R_i\omega_0 = 7.754$ mm/μs. The angular speed ω_0 at which the surface wave sweeps around the arc, after reaching the steady state propagation mode, therefore also drops. Figure 21a shows the D_n variation across the DSD surface for $R_e = 66.5$ mm and $R_e = 67.35$ mm. The drop in D_n globally across the arc is significant relative to the larger R_e cases. We know from the analysis of rate stick and slab geometries [25, 26] that if the propagation speed of the detonation becomes too small the detonation fails, likely due to insufficient chemical energy being released within the detonation driving zone structure for the wave to propagate [2]. However, the exact physical mechanisms are not well understood. In previous work, a PBX 9501 rate stick with 0.79 mm radius detonated with an axial propagation speed of 8.259 mm/μs [25, 26], while a PBX 9501 slab with a thickness of 1 mm detonated with speed 8.461 mm/μs. A slab with thickness 0.8 mm also detonated, but due to the initiation being non-uniform, an axial propagation speed was not evaluated [26]. Thus the failure radius for a PBX 9501 rate stick is less than 0.79 mm, while for a PBX 9501 slab it is less than 0.8 mm [26]. Given the rapid decline in $R_i\omega_0$, and thus ω_0, between $R_e = 66.0$ mm and 65.9 mm for the arc configuration with $R_i = 65.35$ mm, we predict on the basis of the DSD model that the arc thickness for which a PBX 9501 detonation will fail to propagate lies somewhere in range of $0.55 - 0.65$ mm.

Similar behavior to that for $R_i = 65.35$ mm is observed for $R_i = 100.35$ mm (Fig. 20b and 21b). Again, for all values of R_e shown, the surface propagation is steady at the point $\max(\theta_s) = 3\pi/4$. For $R_i = 100.35$ mm, ω_0 is constant when $R_e \gtrsim 103.5$ mm (Fig. 20b). The surface structure senses the presence of the angle (sonic) confinement condition on $r = R_e$ until $R_e > 117.79$ mm (Fig. 21b). Also, $R_i\omega_0 = 8.057$ mm/μs for $R_e = 101.0$ mm, while for $R_e = 100.9$ mm, $R_i\omega_0 = 7.766$ mm/μs. Thus, again, we predict that the PBX 9501 arc thickness for which a detonation will fail to propagate lies somewhere in range of $0.55 - 0.65$ mm for $R_i = 100.35$ mm.
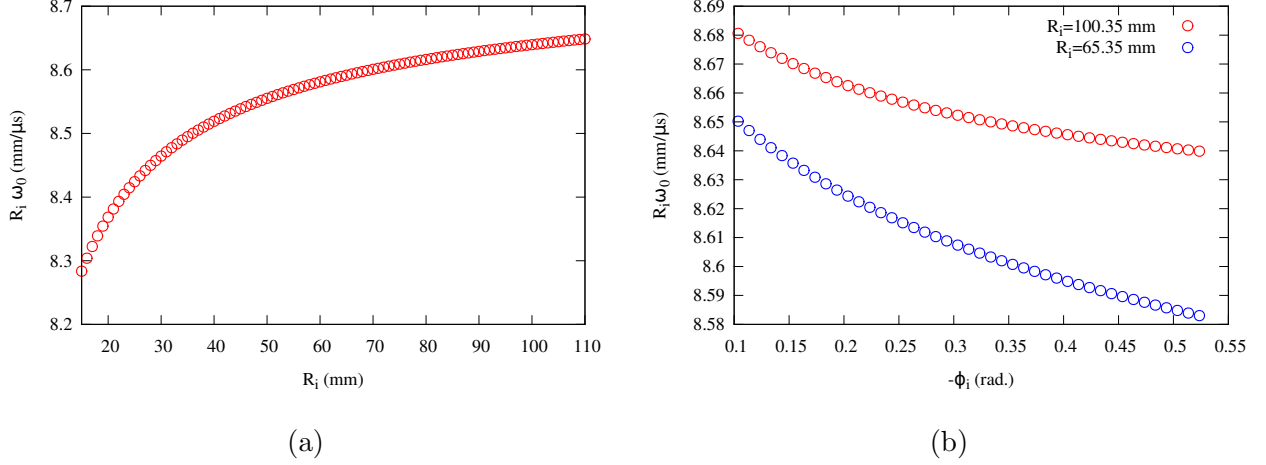
Figure 22: (a) Variation of the steady linear speed $R_i\omega_0$ along the inner arc surface $r = R_i$ with changes in the inner radius R_i for $R_e - R_i = 5$ mm. (b) Variation of the steady linear surface speed $R_i\omega_0$ along $r = R_i$ with changing confinement angle ϕ_i on $r = R_i$ and with $\phi_e = -\phi_i$ on $r = R_e$ for the two arc geometries 65.35 mm x 67.35 mm and 100.35 mm x 120.35 mm.

5.2. Effect of varying inner radius R_i

The effect of varying R_i on the linear detonation speed $R_i\omega_0$ along the inner arc surface at the time when $\max(\theta_s) = 3\pi/4$ is explored in Fig. 22a. Here, the arc thickness is fixed at $R_e - R_i = 5$ mm, with comparable variations found for $R_e - R_i = 10$ mm. As before, for all values of R_i shown, the surface propagation is steady at the point $\max(\theta_s) = 3\pi/4$. For decreasing R_i, i.e. as the curvature of the inner arc surface increases, the role of the second term on the right hand side of the DSD surface curvature term (19), i.e. the rate of change of polar angle with arclength moving along the DSD surface, becomes more significant. The speed $R_i\omega_0$ drops monotonically with decreasing R_i, but even for $R_i = 15$ mm, the linear speed of the PBX 9501 detonation on $r = R_i$ has a value 8.284 mm/µs. We conjecture that an arc of PBX 9501 will therefore detonate for small inner radius values, for which there is a large degree of diffraction.

5.3. Effect of varying confinement

For all cases studied thus far, both the inner and outer surfaces of the PBX 9501 arcs have been unconfined, i.e. $\phi_i = -\phi_s$ and $\phi_e = \phi_s$ in (20) and (21). If the surfaces of the arc were now confined, e.g. with metals [2], the magnitude of ϕ_i and ϕ_e will drop below ϕ_s. In the arc geometry, confinement restricts the degree of curvature that can develop, especially at the inner arc surface. For actual specific confinement materials, the confinement angle can be calculated using shock polar analysis for a given linear phase speed as described in the reviews [43, 2]. Figure 22b shows how the steady linear DSD surface speed on $r = R_i$ is affected by decreasing the magnitude of ϕ_i, with $\phi_e = -\phi_i$ on $r = R_e$ for the two arc geometries 65.35 mm x 67.35 mm and 100.35 mm x 120.35 mm. For the 65.35 mm x 67.35 mm arc, $R_i\omega_0$ increases by 67 m/s increasing ϕ_i from $-\pi/6$ to -0.1 radians. Similarly, for the 100.35 mm x 120.35 mm arc, $R_i\omega_0$ increases by 42 m/s over the same ϕ_i range change.
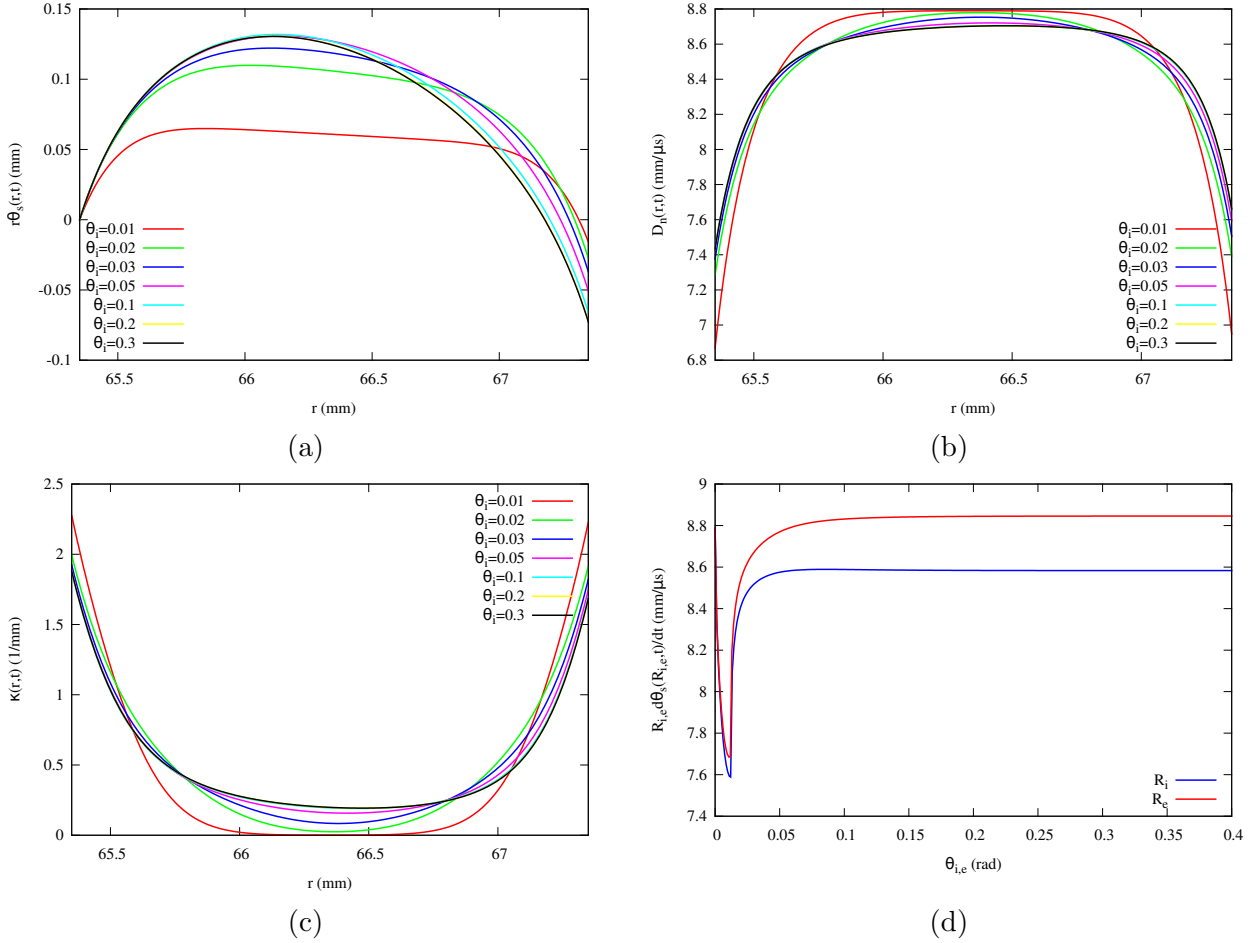
26

Figure 23: Relaxation dynamics of the DSD surface to a steady-state evolution for the 65.35 mm (R_i) vs. 67.35 mm (R_e) arc. Sub-figure (a) shows the surface height variation relative to the inner arc surface in terms of $r\theta_s(r,t)$. The parameter θ_i ($= \theta_s(R_i, t_i)$) indicates the polar angle of the DSD surface point on the inner arc surface at the time the surface shape was extracted. For comparison purposes, all surface shapes have then been shifted such that the point on the inner arc surface is set to a polar angle of zero. For reference purposes, $t_i = 0.0824$ at $\theta_i = 0.01$, $t_i = 0.163$ at $\theta_i = 0.02$, $t_i = 0.240$ at $\theta_i = 0.03$, $t_i = 0.393$ at $\theta_i = 0.05$, $t_i = 0.773$ at $\theta_i = 0.1$, $t_i = 1.535$ at $\theta_i = 0.2$ and $t_i = 2.296$ at $\theta_i = 0.3$. Units of t_i are μs and θ_i are radians. Sub-figures (b) and (c) show the variations in $D_n(r, t_i)$ and $\kappa(r, t_i)$ respectively corresponding to each surface shown in (a). Sub-figure (d) shows the variation in linear speed $R_i d\theta_s(R_i, t)/dt$ as a function of polar angle $\theta_i = \theta_s(R_i, t)$ along $r = R_i$ and $R_e d\theta_s(R_e, t)/dt$ as a function of polar angle $\theta_e = \theta_s(R_e, t)$ along $r = R_e$.

5.4. Relaxation dynamics

Finally, we discuss some of the basic elements of the relaxation dynamics to steady-state propagation using as a basis the three PBX 9501 arc geometries described in [23]. In particular, we describe how the relaxation is influenced by the inner arc radius R_i and thickness $R_e - R_i$. Various aspects of the detonation relaxation dynamics in an arc configuration for other explosives have also been explored recently in [38, 39] using reactive burn modeling. Figure 23 shows the relaxation dynamics of the DSD surface to a steady-state evolution for the thinnest 65.35 mm x 67.35 mm arc. Figure 23a shows the variation in the DSD surface height $r\theta_s(r,t)$ at each r relative to the
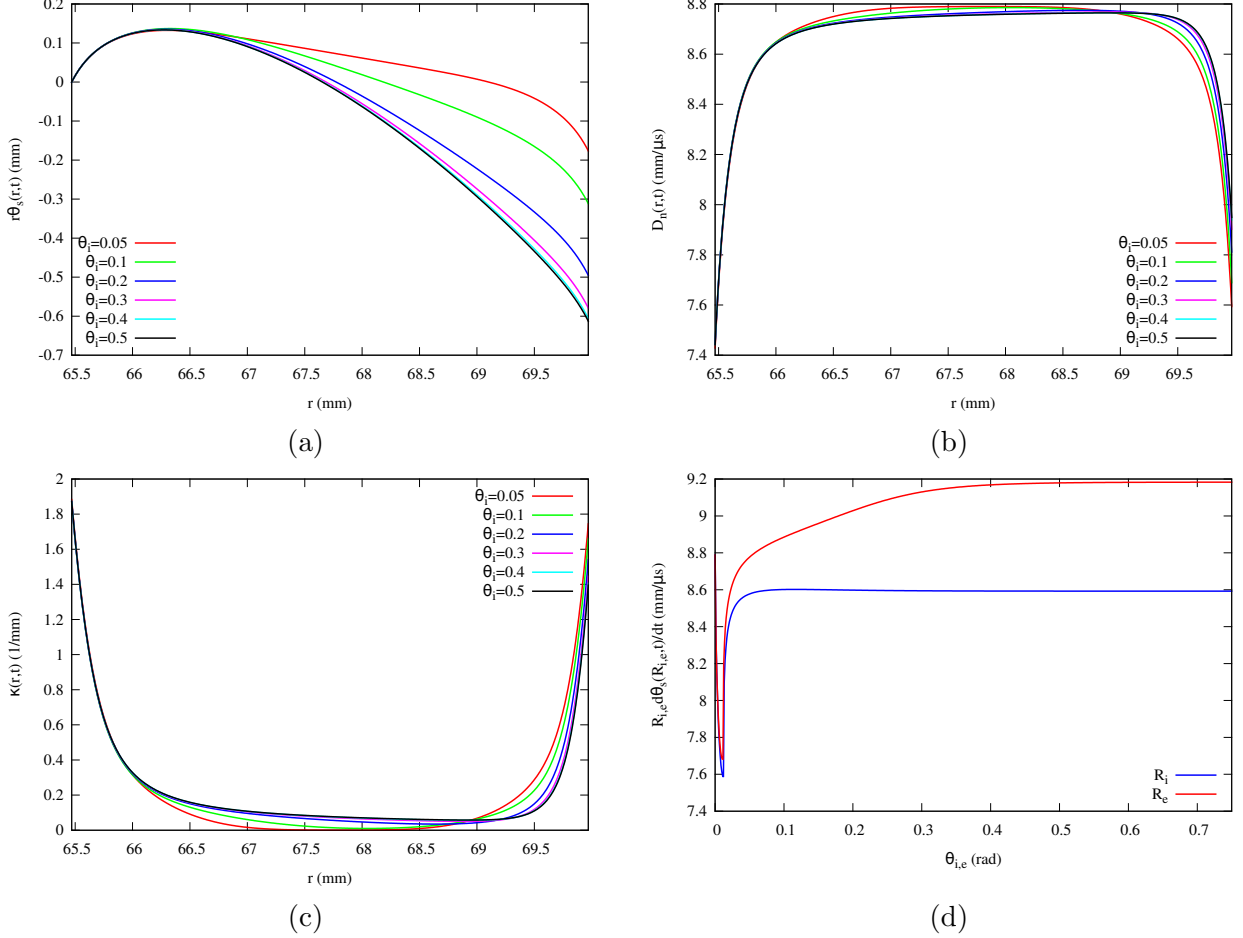
Figure 24: As for Fig. 23, but for the 65.47 mm (R_i) vs. 69.97 mm (R_e) arc. For reference purposes, $t_i = 0.394$ at $\theta_i = 0.05$, $t_i = 0.775$ at $\theta_i = 0.1$, $t_i = 1.536$ at $\theta_i = 0.2$, $t_i = 2.297$ at $\theta_i = 0.3$, $t_i = 3.059$ at $\theta_i = 0.4$ and $t_i = 3.821$ at $\theta_i = 0.5$.

DSD surface position on $r = R_i$. The polar angle of the DSD surface position on $r = R_i$ at the times the profiles are extracted during the evolution is indicated by $\theta_i = \theta_s(R_i, t_i)$, where t_i is the extraction time. Figures 23b,c show the corresponding $D_n(r, t_i)$ and $\kappa(r, t_i)$ profiles. Starting from the flat surface $\theta_s(r, 0) = 0$, the influence of the DSD surface boundary angle on $r = R_i$ and $r = R_e$ propagates into the interior, along with changes that arise due to the wave diffraction process in the arc geometry. We observe the development of layers containing significant changes in D_n and κ along the inner and outer arc boundaries. However, in the small angular segment, $0 < \theta_s(R_i, t) \leq 0.03$, for $0 < t \leq 0.240$ μs, the segment of the DSD surface near $r = R_i$ has already relaxed close to its steady state value. Time-dependent evolution in the outer sections of the arc progress, and these continue to weakly influence the propagation speed of the DSD surface. By $\theta_i = 0.3$, the surface evolution has fully relaxed to steady-state propagation, with the wave subsequently sweeping around the arc with an angular speed of $\omega_0 = 0.1313$ radians/μs. Figure 23d shows the variation in linear speed $R_i d\theta_s(R_i, t)/dt$ as a function of polar angle $\theta_i = \theta_s(R_i, t)$ along $r = R_i$ and $R_e d\theta_s(R_e, t)/dt$ as a function of polar angle $\theta_e = \theta_s(R_e, t)$ along $r = R_e$. The relaxation
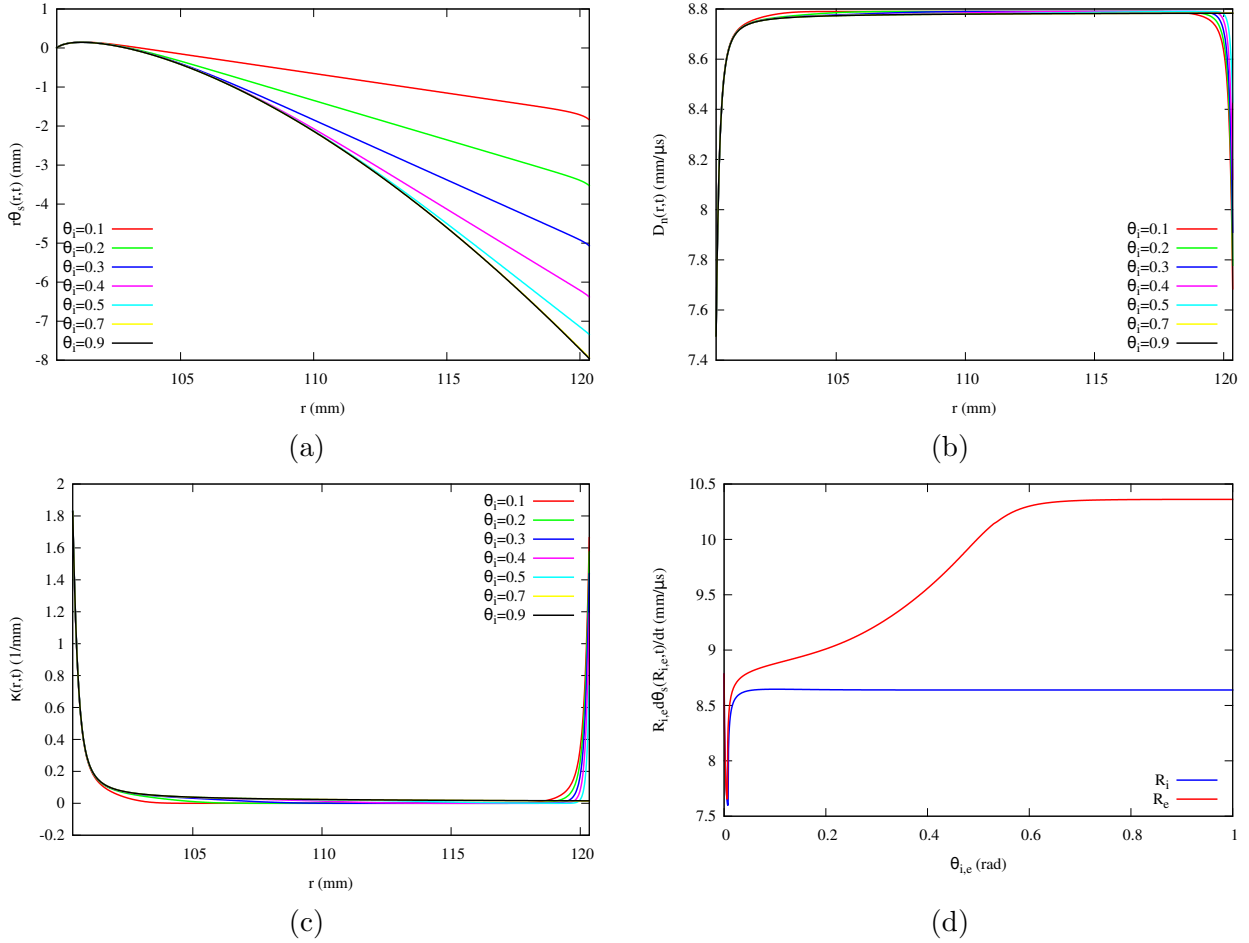
28

(a)

(b)

(c)

(d)

Figure 25: As for Fig. 23, but for the 100.35 mm (R_i) vs. 120.35 mm (R_e) arc. For reference purposes, $t_i = 1.175$ at $\theta_i = 0.1$, $t_i = 2.336$ at $\theta_i = 0.2$, $t_i = 3.497$ at $\theta_i = 0.3$, $t_i = 4.659$ at $\theta_i = 0.4$, $t_i = 5.820$ at $\theta_i = 0.5$, $t_i = 8.143$ at $\theta_i = 0.7$, and $t_i = 10.466$ at $\theta_i = 0.9$.

times to steady-state propagation along $r = R_i$ and $r = R_e$ are comparable, with the evolution along $r = R_i$ relaxing slightly faster than for $r = R_e$, corresponding to the observed relaxation processes in Fig. 23a-c.

The relaxation process for the 65.47 x 69.97 mm arc geometry is shown in Fig. 24. The inner arc region again relaxes rapidly, so that at the polar angle $\theta_i = 0.05$ on $r = R_i$, the DSD surface near the inner arc surface has already relaxed close to its steady-state evolution profile (Fig 24a). At $\theta_i = 0.1$, the linear speed $R_i d\theta_s(R_i, t)/dt$ on $r = R_i$ has reached its steady-state value (Fig. 24d), and a boundary layer characterized by rapid variations in D_n and κ at the inner surface have fully formed (Fig. 24b,c). Due to the thicker arc dimension, with $R_e - R_i = 4.5$ mm, the outer section of the arc has a significantly longer relaxation period, and only by $\theta_e = 0.6$ has the linear speed $R_e d\theta_s(R_e, t)/dt$ on $r = R_e$ has reached its steady-state value (Fig. 24d). A second boundary layer characterized by rapid variations in D_n and κ has also formed near the outer arc boundary $r = R_e$ (Fig. 24b,c). The relaxation process for the 100.35 x 120.35 mm arc geometry is shown in Fig. 25. Similar evolutionary dynamics are observed to the 65.47 x 69.97 mm arc geometry. The

slow relaxation period of the outer section of the 20 mm thick arc is clearly evident (Fig. 25d), and only by $\theta_e = 0.9$ has the linear speed $R_e d\theta_s(R_e, t)/dt$ on $r = R_e$ reached its steady-state value (Fig. 25d). The boundary layer structure near $r = R_i$ described in [21] is prominent (Fig. 25b,c), with $D_n \approx D_{CJ}$ and κ small in the central section of the arc. For steady-state propagation, the surface continuation condition in (21) is activated, and the boundary layer in D_n and κ near $r = R_e$, observed at earlier times during the relaxation process, disappears as steady-state evolution is approached.

6. Summary

We have developed a surface evolution model for the detonation propagation dynamics of the conventional high explosive PBX 9501, a plastic bonded explosive composed of 95.0 weight (wt.)% HMX explosive crystals with a binder mixture of 2.5 wt.% Estane and a 2.5 wt.% eutectic mixture of BDNPA/BDNPF. The evolution model is based on the concept of detonation shock dynamics, which relates the normal surface speed D_n to its local surface curvature κ. The detonation properties of PBX 9501 are broadly similar to many other conventional high explosives, and therefore our work on PBX 9501 is a surrogate for understanding the influence of curvature on propagation in these types of explosives. Surface evolution models are important for the understanding and modification of engineering design calculations for high explosive applications.

In the current article, we have described a series of unconfined PBX 9501 slab geometry experiments of varying thickness (T), and detailed how the steady axial detonation speed and detonation front shape data are obtained as a function of T. A merit-function based calibration process is then described that uses the PBX 9501 thickness effect variation and the front-shape data to parametrize the $D_n - \kappa$ propagation law, as well as to obtain the surface normal angle that is applied at the HE boundary for unconfined charges. Our calibration process ensures a balance between fitting the front-shape data and steady axial detonation speeds, both of which are important to the performance of a $D_n - \kappa$ model when applied to different geometries. As a by-product of the analysis, we showed that the inherent noise in the front-shape data can be related to the degree of crystal-binder heterogeneity in the explosive. Application of the newly derived PBX 9501 $D_n - \kappa$ surface propagation law to existing diameter effect data on PBX 9501, based on a cylindrical rate-stick geometry, was shown to predict speeds higher than those obtained experimentally, although we noted concerns about differences in material lots between the slab and rate stick test series, as well as inherent variability in experimental measurements of propagation speed for charges at nominally the same density and radii.

We then described the application of the time-dependent PBX 9501 $D_n - \kappa$ surface evolution law to detonation wave propagation in two-dimensional circular arc geometries, based on experiments described in [23]. The circular arc configuration is the simplest geometry that accounts for modifications of the detonation front curvature induced by diffraction, and provides a stringent test for $D_n - \kappa$ based modeling. The arc experiments in [23] used the same lot of PBX 9501 as the slab geometry experiments described here. Solutions of the PBX 9501 DSD model developed here were then compared with those determined experimentally. Excellent agreement of both the linear speeds on the inner and outer arc surfaces were found, as well as those of the detonation front shapes predicted by the DSD model, for all three PBX 9501 arc geometries.

In the current article, we have also systematically examined the effect of arc thickness, inner radius, confinement effects and relaxation dynamics to steady-state propagation for PBX 9501 arc

geometries. For a fixed inner radius R_i and for an arc thickness larger than only a few millimeters, the angular speed ω_0 at which the surface sweeps around the arc, after reaching steady-state propagation, does not depend on the arc thickness. The surface structure, however, still senses the presence of the angle (sonic) confinement condition on the outer arc surface $r = R_e$ for much thicker arcs. For example, for $R_i = 65.35$ mm, ω_0 becomes constant when $R_e \gtrsim 68$ mm, while the surface structure senses the presence of the angle condition on $r = R_e$ until $R_e > 77.1$ mm. Thus PBX 9501 detonations follow the general theory developed in [21], where for sufficiently wide arcs, ω_0 is determined by the surface curvature variations in a boundary layer attached to the inner arc surface, characterized by rapid variations in $D_n(r, t)$ and $\kappa(r, t)$ near $r = R_i$. For arcs thinner than a couple of millimeters, the detonation speed drops off rapidly. We predicted that for the $R_i = 65.35$ mm and $R_i = 100.35$ inner radius arcs [23], a detonation would not propagate for arc thicknesses smaller than $0.55 - 0.65$ mm.

We also demonstrated that PBX 9501 will, in principle, detonate in charges with small R_i, where the curvature of the inner arc surface is large. Confinement effects, obtained by varying the surface normal angle along $r = R_i$ and $r = R_e$, are also shown to be significant in the arc geometry. Finally, we showed that the relaxation dynamics of PBX 9501 detonation to steady-state propagation are significantly affected by the arc thickness, with the inner layers of the DSD surface near $r = R_i$ relaxing rapidly, and outer layers of the surface relaxing on a larger time scale. In all cases, our DSD surface evolution model provides a significant improvement over a Huygens surface wave propagation model, where $D_n = D_{CJ}$, as commonly used for engineering applications of a number of conventional high explosives.

In future studies, we will combine the surface evolution model developed here for PBX 9501 detonation with the pseudo-reaction-zone (PRZ) model for energy delivery dynamics. The calibration procedure for the PRZ model that would sync the energy release to the PBX 9501 surface evolution model is described in [50]. Higher-order DSD models that incorporate acceleration [17] and transverse flow effects [47, 26] could also be examined, given the large values of κ reached in the boundary layer structures. However, comparisons of the base $D_n - \kappa$ model with experiments for arc geometries described in [23] show that these effects are likely to be of secondary importance, at least for the arc geometry. We also envision additional experiments to measure shot-to-shot variability with PBX 9501 detonation using charges with the same density and lot specification, particularly focusing on potential heterogeneous effects when the charge size becomes comparable to the HMX crystal size.

References

[1] L. Davison, Fundamentals of shock wave propagation in solids, Springer Science, 2008.

[2] M. Short, J. Quirk, High explosive detonation-confiner interactions, Annu. Rev. Fluid Mech. 50 (2018) 215–242.

[3] J. Bdzil, M. Short, Theory of Mach reflection of detonation at glancing incidence, J. Fluid Mech. 811 (2017) 269–314.

[4] I. Golombek, J. Niemeyer, A model for multidimensional delayed detonations in SN Ia explosions, Astron. & Astrophy. 438 (2005) 611–616.

[5] M. Fink, W. Hillebrandt, F. Röpke, Double-detonation supernovae of sub-Chandrasekhar mass white dwarfs, Astron. & Astrophy. 476 (2007) 1133–1143.

[6] D. Wiggins, S. Falle, Two-dimensional detonation waves in Type 1a supernovae, Mon. Not. R. Astron. Soc. 287 (1997) 575–582.

[7] R. Pramanik, D. Deb, Implementation of smoothed particle hydrodynamics for detonation of explosive with application to rock fragmentation, Rock Mech. Rock Eng. 48 (2015) 1683–1698.

[8] I. Onederra, J. Furtney, E. Sellers, S. Iverson, Modelling blast induced damage from a fully coupled explosive charge, Int. J. Rock Mech. and Mining Sci. 58 (2013) 73–84.

[9] B. Zakrisson, B. Wikman, H. Häggblad, Numerical simulations of blast loads and structural deformation from near-field explosions in air, Int. J. Impact Eng. 38 (2011) 597–612.

[10] M. Price, V. Nguyen, O. Hassan, K. Morgan, A method for compressible multimaterial flows with condensed phase explosive detonation and airblast on unstructured grids, Comput. Fluids 111 (2015) 76–90.

[11] D. Stewart, N. Glumac, F. Najjar, M. Szuck, Hydrodynamics computation of jet formation and penetration for micro-shaped charges, Procedia Engineer. 58 (2013) 39 – 47.

[12] J. B. Bdzil, D. S. Stewart, Modeling two-dimensional detonations with detonation shock dynamics, Phys. of Fluids A: Fluid Dyn. 1 (1989) 1261.

[13] J. B. Bdzil, D. S. Stewart, Time-dependent two-dimensional detonation: the interaction of edge rarefactions with finite-length reaction zones, J. Fluid Mech. 171 (1986) 1–26.

[14] D. S. Stewart, J. B. Bdzil, The shock dynamics of stable multidimensional detonation, Combust. Flame 72 (1988) 311–323.

[15] D. S. Stewart, J. B. Bdzil, A lecture on detonation-shock dynamics, in: J. Buckmaster, T. Takeno (Eds.), Mathematical Modeling in Combustion Science, Springer, 1988, pp. 17–30.

[16] J. Bdzil, W. Fickett, D. Stewart, Detonation shock dynamics: A new approach to modeling multi-dimensional detonation waves, in: Ninth Symposium (International) on Detonation, Office of the Chief of Naval Research, OCNR 113291-7, 1989, pp. 730–742.

[17] D. Lambert, D. Stewart, S. Yoo, B. Wescott, Experimental validation of Detonation Shock Dynamics in condensed explosives, J. Fluid Mech. 546 (2006) 227–253.

[18] S. Dunkley, G. Sharpe, S. Falle, Detonation shock dynamics of Type Ia supernovae, Mon. Not. Roy. Astron. Soc. 431 (2013) 3429–3443.

[19] A. N. Hodgson, Modelling an IHE experiment with a suite of DSD models, in: Journal of Physics Conference Series, volume 500, 2014, p. 052018.

[20] B. Lieberthal, J. Bdzil, D. Stewart, Modelling detonation of heterogeneous explosives with embedded inert particles using detonation shock dynamics: Normal and divergent propagation in regular and simplified microstructure, Combust. Theory Modell. 18 (2014) 204–241.

[21] M. Short, J. Quirk, C. Meyer, C. Chiquete, Steady detonation propagation in a circular arc: a Detonation Shock Dynamics model, J. Fluid Mech. 807 (2016) 87–134.

[22] B. Lieberthal, D. Stewart, A. Hernández, Geometrical shock dynamics applied to condensed phase materials, J. Fluid Mech. 828 (2017) 104–134.

[23] M. Short, E. Anderson, C. Chiquete, S. Jackson, Experimental and modeling analysis of detonation in circular arcs of the conventional high explosive PBX 9501, Proc. Combust. Institut. Accepted (2020).

[24] A. J. Higgins, Discrete effects in energetic materials, in: Journal of Physics Conference Series, volume 500, 2014, p. 052016.

[25] A. W. Campbell, R. Engelke, The diameter effect in high-density heterogenous explosives, in: Sixth Symposium (International) on Detonation, Office of Naval Research, ACR-221, 1976, pp. 642–652.

[26] S. I. Jackson, M. Short, Scaling of detonation velocity in cylinder and slab geometries for ideal, insensitive and non-ideal explosives, J. Fluid Mech. 773 (2015) 224–266.

[27] R. Engelke, J. B. Bdzil, A study of the steady-state reaction-zone structure of a homogeneous and a heterogeneous explosive, Phys. Fluids 26 (1983) 1210.

[28] C. B. Skidmore, D. S. Phillips, P. M. Howe, The evolution of microstructural changes in pressed HMX explosives, in: Eleventh International Detonation Symposium, Office of Naval Research, ONR 33300-5, 1998, pp. 556–564.

[29] C. B. Skidmore, D. S. Phillips, S. F. Son, B. W. Asay, Characterization of HMX particles in PBX 9501, in: AIP Conference Proceedings, volume 429, 1998, pp. 579–582.

[30] R. L. Gustavsen, S. A. Sheffield, R. R. Alcon, L. G. Hill, Shock initiation of new and aged PBX 9501, in: Twelth International Detonation Symposium, Office of Naval Research, ONR 333-05-2, 2002, pp. 530–537.

[31] H. Nakayama, T. Moriya, J. Kasahara, A. Matsuo, Y. Sasamoto, I. Funaki, Stable detonation wave propagation in rectangular-cross-section curved channels, Combust. Flame 159 (2012) 859–869.

[32] H. Nakayama, J. Kasahara, A. Matsuo, I. Funaki, Front shock behavior of stable curved detonation waves in rectangular-cross-section curved channels, Proc. Combust. Instit. 34 (2013) 1939–1947.

[33] V. Rodriguez, C. Jourdain, P. Vidal, R. Zitoun, An experimental evidence of steadily-rotating overdriven detonation, Combust. Flame 202 (2019) 132–142.

[34] M. Short, C. Chiquete, J. Quirk, Propagation of a stable gaseous detonation in a circular arc configuration, Proc. Combust. Instit. 37 (2019) 3593–3600.

[35] P. Souers, S. Anderson, B. Hayes, J. Lyle, E. Lee, S. McGuire, C. Tarver, Corner turning rib tests on LX-17, Propell. Expl. Pyrotechn. 23 (1998) 200–207.

[36] T. Zhao, Q. Li, F. Zhao, C. Sun, L. Han, Z. He, W. Gao, An experimental study of detonation propagation in the arc insentitive high explosive initiated on the basal plane, in: Eleventh International Detonation Symposium, Office of Naval Research, ONR 333000-5, 1998, pp. 1023–1028.

[37] S. Lubyatinsky, S. Batalov, A. Y. Garmashev, V. Israelyan, O. Kostitsyn, B. Loboiko, V. Pashentsev, V. Sibilev, E. Smirnov, V. Filin, Detonation propagation in 180° ribs of an insensitive high explosive, in: AIP Conference Proceedings, volume 706, 2003, pp. 859–862.

[38] E. Ioannou, S. Schoch, N. Nikiforakis, L. Michael, Detonation propagation in annular arcs of condensed phase explosives, Phys. Fluids 29 (2017) 116102.

[39] M. Short, J. Quirk, C. Chiquete, C. Meyer, Detonation propagation in a circular arc: reactive burn modelling, J. Fluid Mech. 835 (2018) 970–998.

[40] M. Short, C. Chiquete, J. Bdzil, J. Quirk, Detonation diffraction in a circular arc geometry of the insensitive high explosive PBX 9502, Combust. Flame 196 (2018) 129–143.

[41] L. G. Hill, J. B. Bdzil, W. C. Davis, R. Engelke, D. L. Frost, Front curvature analysis and detonation shock dynamics calibration for pure and sensitized nitromethane, in: AIP Conference Proceedings, volume 505, 2000, pp. 813–816.

[42] R. A. Catanach, L. G. Hill, Diameter effect curve and detonation front curvature measurements for ANFO, in: AIP Conference Proceedings, volume 620, 2001, pp. 906–909.

[43] J. Bdzil, D. Stewart, The dynamics of detonation in explosive systems, Ann. Rev. Fluid Mech. 39 (2007) 263–292.

[44] D. Stewart, J. Bdzil, Examples of detonation shock dynamics for detonation wave spread applications, in: Ninth Symposium (International) on Detonation, Office of the Chief of Naval Research, OCNR 113291-7, 1989, pp. 773–783.

[45] J. Bdzil, W. Davis, Time-Dependent Detonations, Technical Report LA-5926-MS, Los Alamos National Laboratory, Los Alamos, NM, USA, 1975.

[46] S. Jackson, M. Short, Determination of the velocity-curvature relationship for unknown front shapes, in: AIP Conference Proceedings, volume 1426, 2012, pp. 347–350.

[47] J. B. Bdzil, T. D. Aslam, R. A. Catanach, L. G. Hill, M. Short, DSD front models: non-ideal explosive detonation in ANFO, in: Twelth International Detonation Symposium, Office of Naval Research, ONR 333-05-2, 2002, pp. 409–417.

[48] J. J. Moré, The Levenberg-Marquardt algorithm: implementation and theory, in: Numerical analysis, Springer, 1978, pp. 105–116.

[49] T. D. Aslam, Detonation shock dynamics calibration of PBX 9501, in: AIP Conference Proceedings, volume 955, 2007, pp. 813–816.

[50] C. Chiquete, M. Short, C. Meyer, J. Quirk, Calibration of the pseudo-reaction-zone model for detonation wave propagation, Combust. Theory Modell. 22 (2018) 744–776.